Polarized spectroscopy of Sm3+ ions in monoclinic KGd(WO4)2 crystals for lasers emitting in the red

Amandine Baillard, Pavel Loiko, Daniel Rytz, Sebastian Schwung, Anatoly Pavlyuk, Alexey Kornienko, Elian Pimor, Moritz Badtke, Christian Kränkel, Elena Dunina, et al.

Polarized spectroscopy of Sm^{3+} ions in monoclinic $KGd(WO_4)_2$ crystals for red lasers

Amandine Baillard[a], Pavel Loiko[a], Daniel Rytz[b], Sebastian Schwung[b], Anatoly Pavlyuk[c], Alexey Kornienko[d], Elian Pimor[a], Moritz Badtke[e], Christian Kränkel[e], Elena Dunina[d], Liudmila Fomicheva[f], Michaël Fromager[a], Alain Braud[a] and Patrice Camy[a,*]

[a]Centre de Recherche sur les Ions, les Matériaux et la Photonique (CIMAP), UMR 6252 CEA-CNRS-ENSICAEN, Université de Caen Normandie, 6 Boulevard Maréchal Juin, 14050 Caen Cedex 4, France
[b]EOT GmbH, Struthstraße 2, D-55743, Idar-Oberstein, Germany
[c]A.V. Nikolaev Institute of Inorganic Chemistry, Siberian Branch of Russian Academy of Sciences, 3 Lavrentyev Ave., Novosibirsk, Russia 630090
[d]Vitebsk State Technological University, 72 Moskovskaya Ave., 210035 Vitebsk, Belarus
[e]Leibniz-Institut für Kristallzüchtung (IKZ), Max-Born-Str. 2, 12489 Berlin, Germany
[d]BIP - University of Law and Social-Information Technologies, Department of IT and Mathematics, 3 Korol St., 220004 Minsk, Belarus
**Corresponding author, e-mail: patrice.camy@ensicaen.fr*

Abstract: Single-crystals of potassium gadolinium double tungstate $KGd(WO_4)_2$ doped with Sm^{3+} ions up to 20 at.% were grown from the flux using $K_2W_2O_7$ as a solvent and a detailed polarization-resolved spectroscopic study of Sm^{3+} ions was performed with the goal of developing novel materials for visible lasers. Polarized absorption spectra were measured and 4f-4f transition intensities of Sm^{3+} ions were calculated using a modified Judd-Ofelt theory yielding the intensity parameters of Ω_2 = 8.027, Ω_4 = 7.210 and Ω_6 = 2.322 [10^{-20} cm^2] and α = -0.017 [10^{-4} cm]. Polarized stimulated-emission properties of Sm^{3+} ions were studied. For the $^4G_{5/2} \rightarrow {}^6H_{9/2}$ transition in the red, the maximum σ_{SE} is 0.55×10^{-20} cm^2 at 649.0 nm for light polarization $\boldsymbol{E} \parallel N_p$ (luminescence branching ratio: 40.2%). The radiative lifetime of the $^4G_{5/2}$ state is 734 μs. The luminescence dynamics from this manifold was analyzed using the Inokuti-Hirayama model. The possible role of 4f – 4f excited-state absorption from the $^4G_{5/2}$ level in preventing laser operation in the orange and deep red is analyzed. A 0.8 at.% Sm:$KGd(WO_4)_2$ laser generated an output power of 37.8 mW at 649 nm, with a laser threshold of 87 mW and a slope efficiency of 17.6%.

Keywords: samarium ions; tungstate crystals; luminescence, Judd-Ofelt theory; visible lasers.

1. Introduction

The rare-earth (RE) element samarium $_{62}$Sm was first isolated from the mineral *samarskite* by the French chemist Lecoq de Boisbaudran in 1879 [1]. Trivalent samarium ions Sm^{3+} possess an electronic configuration of [Xe]$4f^5$, with two groups of short-living LS-split manifolds ^6H_J (J = 5/2 – 15/2), with $^6H_{5/2}$ being the ground-state, and ^6F_J (J = 1/2 – 11/2) at energies between 0 and 11000 cm^{-1}. Among the higher lying energy manifolds in the energetic range below 50000 cm^{-1} (corresponding to 200 nm ground state absorption), $^4G_{5/2}$ is the only metastable state with a lifetime suitable to serve as an upper laser level.

As depicted in the energy-level scheme in Fig. 1, Sm^{3+} ions provide multi-color emissions at several transitions in the visible ranging from the yellow to the deep red spectral range as well as near-infrared emission lines and are thus an interesting candidate for the above mentioned applications. All visible emission lines in Sm^{3+} originate from the $^4G_{5/2}$ manifold, which exhibits a long luminescence lifetime (from a few hundred of µs to a few ms). Due to the relatively large energy gap to the next lower-lying energy levels of about 7400 cm^{-1}, the rate of non-radiative transitions from the $^4G_{5/2}$ manifold is very weak, even in high-phonon-energy matrices such as oxides [2-3].

Nowadays, Sm^{3+}-doped materials are mainly used as red phosphors for white LEDs with good color rendering index [4]. They also find applications in medical imaging for radiation dosimetry, remote sensing, and visual display devices [5-7].

Sm^{3+} ions are also of interest for visible lasers. There are two main challenges when developing laser sources employing Sm^{3+}-doped materials. First, self-quenching caused by several cross-relaxation (CR) channels (*cf*. Fig. 1), resulting in a strong reduction of the luminescence lifetime of the $^4G_{5/2}$ emitting state upon increasing the doping concentration. This behavior tends to limit the accessible doping levels for laser gain [2,8,9]. Second, excited-state absorption (ESA) into higher lying energy levels of the 4f configuration is present at the potential laser wavelengths. Sm^{3+} ions exhibit a very complex energy-level scheme, with a total 198 energy manifolds of the $4f^5$ configuration splitting into 1001 two-fold degenerate Stark levels in suitable host crystals and extending up to energies of about 125000 cm^{-1}. Thus, the risk of 4f-4f ESA transitions must be considered, to limit or even inhibit laser emission at specific transitions [2]. Fortunately, parity allowed ESA transitions into energy levels of the $4f^45d^1$ excited configuration of Sm^{3+} should not occur, as these are located at much higher energies than the $4f^5$ levels. Thus, the corresponding ESA transitions should not prevent laser action in the visible [10].

The first laser (*optical maser*) action using a rare-earth ion was achieved in 1961 by using a CaF_2 crystal doped with divalent samarium ions Sm^{2+}. Sorokin and Stevenson generated a deep-red laser emission at 708 nm under Xe flashlamp pumping at low temperature (LT) [11]. In 1979, Kazakov *et al.* demonstrated the first laser action using trivalent samarium ions Sm^{3+}, generating an orange laser emission at 593 nm also at LT. The active medium was a self-activated Sm:TbF_3 crystal, which enhanced the broad-band pump absorption through energy transfer from Tb^{3+} to Sm^{3+} [12]. In the late 1980s, researchers from the University of Southampton obtained the first Sm^{3+}-based laser action at room temperature (RT) using Sm^{3+}-doped silica glass fibers pumped by an argon ion laser. The laser operated in the red at 651 nm, with almost 30 mW of output power in the continuous-wave (CW) operation and also demonstrated Q-switched pulse laser operation [13,14]. In 1995, Jenssen reported on orange CW laser emission at 605 nm from a self-activated Sm^{3+}:$LiTbF_4$ crystal at room temperature, generating almost 200 mW of output power with a slope efficiency of 20% whilst with a very high laser threshold of 350 mW [15].

Unfortunately, the ground state absorption from the $^6H_{5/2}$ manifold into the emitting level $^4G_{5/2}$ and all other levels absorbing in the visible is spin-forbidden. Consequently, Sm^{3+} ions exhibit weak absorption in the visible spectral range, and the lack of suitable pump sources in

the blue has greatly restricted the further investigations of Sm lasers. There has been a renewed interest for Sm^{3+}-doped materials since the invention of blue GaN-based laser diodes (awarded by the Nobel Prize in Physics in 2014) [16], and frequency-doubled optically pumped semiconductor lasers (2*ω*-OPSL) [17], which are now commercially available. These technologies have enabled further development of visible lasers based on various rare-earth ions [2,9].

Using a 2*ω*-OPSL as pump source, Marzahl *et al.* achieved laser action in the orange, red and deep-red spectral ranges using both fluoride and oxide host crystals, namely $LiLuF_4$ and $SrAl_{12}O_{19}$. The best laser performance (*i.e.*, the highest output power and slope efficiency and lowest laser threshold) was observed for the fluoride host. With both crystals, the lasers exhibited a self-pulsing behavior, delivering µs-long pulses with a repetition rate in the kHz range. This behavior was attributed to possible ESA at the laser wavelengths [18]. Relatively low laser thresholds were observed for these Sm^{3+} lasers, enabled by the long luminescence lifetime of the $^4G_{5/2}$ emitting level of Sm^{3+}, especially in fluoride matrices, and the four-level laser scheme for the considered transitions. Recently, we reported on the first laser operation of a Sm^{3+}:$KGd(WO_4)_2$ double tungstate crystal in the red, at 649 nm, yielding 18 mW of output power with a slope efficiency of 17%, and a very low laser threshold of only 29 mW. Similarly to the results of Marzahl *et al*. reported in [18], the red laser exhibited a self-pulsing behavior attributed to non-resonant 4f-4f ESA into short-living states [19]. However, the pulse dynamics was rather regular resembling passive Q-switching by a “fast” saturable absorber.

Laser sources directly emitting in the visible find multiple applications in our everyday life, including headlights, display technologies, optical data storage devices, and underwater communication. Moreover, they have many applications in technical fields. In medicine, visible lasers are employed in photoimmune therapy, medical imaging (*e.g.*, Laser Speckle Contrast Imaging), dosimetry, oximetry, and dentistry [20-23]. They are also used in high-resolution microscopy. In fact, the Nobel Prize in Chemistry in 2014 was awarded for the development of “ultra-high resolution fluorescence microscopy”, which was made possible by the use of visible lasers. These lasers are also found in biology, such as genomics, to collect and study tissue samples. Mass spectrometry technics employ such lasers for matrix assisted laser desorption / ionization for measuring the molecular weight of bio-macromolecules [2,18,24,25]. More specifically, yellow and orange lasers are of great interest for quantum optics (for optical clocks) [26], skin treatment and ophthalmology [20,27], and astronomy for developing laser guide star systems (*i.e.*, artificial stars) [28].

The crystal family of monoclinic potassium rare-earth double tungstates with a chemical formula $KR(WO_4)_2$ (where R stands for Y, Gd, or Lu) is a well-known class of host crystals for elaborating solid-state lasers based on RE^{3+} ions, in various geometries and operation regimes, mainly for near-IR emissions [29]. These materials feature a single type of substitution site for RE^{3+} ions as well as high possible doping levels (often up to a stoichiometric composition). Moreover, it provides large distances between neighboring RE^{3+} ions, leading to weak concentration quenching of luminescence. Finally, enabled by the low site symmetry C_2 for RE^{3+} ions, it features high absorption and stimulated-emission cross-sections and a strong anisotropy of absorption and emission properties in polarized light. Also, monoclinic $KR(WO_4)_2$ crystals exhibit a nearly athermal behavior for certain crystal cuts.

Despite the enormous use of monoclinic double tungstates in near-IR lasers, so far, only a few studies addressed their applications for visible laser development. In 2000, Kaminskii *et al.* obtained pulsed laser action in the yellow and red spectral ranges with both $KY(WO_4)_2$ and $KGd(WO_4)_2$ crystals doped with Dy^{3+}, under Xe flashlamp pumping at cryogenic temperatures [30]. In 2013, pulsed laser action in the deep red was achieved at room temperature employing Eu^{3+}-doped $KGd(WO_4)_2$ and $KY(WO_4)_2$ crystals [31,32]. Recently, Loiko *et al*. reported on a deep-red Eu laser based on a stoichiometric $KEu(WO_4)_2$ crystal delivering a Watt-level output

(1.11 W) at 703 nm with a slope efficiency of 43.2% under pumping in the green at 532 nm [33].

In the present work, we report on a detailed polarization-resolved spectroscopic study of Sm^{3+}-doped $KGd(WO_4)_2$ crystals with the goal of developing visible lasers.

2. Experimental

2.1. Crystal growth

Like for other compounds in the monoclinic double tungstate crystal family, the complexity of the growth of $KGd_{1-x}Sm_x(WO_4)_2$ crystals arise from a polymorphic phase transition below the melting point (~1080 °C). Indeed, above ~1005 °C, this crystal has an orthorhombic structure which is a derivative of that of the double molybdate $KY(MoO_4)_2$, denoted as β-phase [34]. However, the low-temperature monoclinic α-phase is the desired phase for laser development. Thus, this crystal cannot be grown from the melt, *e.g.* using the Czochralski method. In the present work, Sm^{3+}-doped $KGd(WO_4)_2$ crystals were grown from the flux lowering the growth temperature below the phase transition temperature.

Low-doped (0.4 at.% and 0.8 at.% Sm, with respect to Gd) Sm:$KGd(WO_4)_2$ crystals were grown at EOT GmbH, Germany. The top-seeded solution growth (TSSG) method was used employing potassium ditungstate $K_2W_2O_4$ as a solvent. The staring materials were K_2CO_3, WO_3, Gd_2O_3, and Sm_2O_3 of high purity (99.99%). They were weighed according to a solute-to-solvent molar ratio close to 1:5. The growth was performed in a platinum crucible in air. The growth charge was melted at 970 °C and well homogenized at this temperature for 24 h. The growth started at about 955 °C, and crystallization was initiated by introducing an [010]-oriented seed from an undoped $KGd(WO_4)_2$ crystal into the melt. Further details about the growth and the cooling process can be found elsewhere [35]. After the crystal growth was completed, the crystal was pulled out from the liquid and slowly cooled down to room temperature. Figure 2(a) presents a photograph of an as-grown 0.8 at.% Sm:$KGd(WO_4)_2$ single-crystal. It is transparent and nearly colorless. The dimensions of the crystal are about 20×25×35 mm^3. Under UV lamp illumination, the crystal exhibits bright orange luminescence, Fig. 2(b).

A second, heavily-doped 20 at.% Sm:$KGd(WO_4)_2$ crystal was grown at NIIC, Russia. A modification of the standard TSSG method, referred to as a low-temperature gradient (LTG) method, was applied [36]. Potassium ditungstate $K_2W_2O_4$ was also employed as a solvent and an [010] oriented seed from undoped $KGd(WO_4)_2$ was used. The growth was also performed in a platinum crucible (Ø 70 mm × 120 mm) in air using a crystal growth station with a weigh control. The crucible was covered with an inverted funnel shaped platinum lid to improve the crystal quality. The lid served as a radiation screen and a diffusion lock for volatile substances, which prevented excessive evaporation and decomposition of the flux. Both the radial and axial thermal gradients inside the crucible were in the range of ~0.1-1 °C/cm. Such an approach could lead to poor dynamical stability. To prevent it, the weighting system serving as electronic feedback was applied (with a precision of 10 mg in the 1 kg range). During the growth, the pulling rate was about 2 to 4 mm/day and the rotation speed was 40-60 rpm.

Figure 2(c) presents a photograph of an as-grown 20 at.% Sm:$KGd(WO_4)_2$ single-crystal. It shows a strong yellow coloration due to the heavy Sm^{3+} doping. The upper part of the crystal boule has a pyramidal shape, and it is determined by prismatic faces {110} and {011} (here and below, we use the notations of the non-standard *I*2/*c* crystallographic setting). The lateral sides of the prismatic part of the boule are also determined by the {110}, {011} faces and pinacoidal {100}, {001} faces. The endface of the boule is determined mainly by the well-developed pinacoidal {010} face that is surrounded with four relatively small {110}, {011} faces.

Thus, the doping levels of the samples available for the experiments presented in the following were 0.4 at.% Sm (ion density: N_{Sm} = 0.248×10^{20} at/cm^3), 0.8 at.% Sm (N_{Sm} = 0.496×10^{20} at/cm^3), and 20 at.% Sm (N_{Sm} = 12.4×10^{20} at/cm^3).

Pure $KGd(WO_4)_2$ crystallizes in the monoclinic space group C^6_{2h} – *C*2/*c*, with the lattice parameters *a* = 10.652 Å, *b* = 10.374 Å, *c* = 7.582 Å, and the monoclinic angle *β* = ***a*** ^ ***c*** = 130.80°, see Fig. 2(d) [37]. Monoclinic $KGd(WO_4)_2$ is optically biaxial, and its optical properties are described within the optical indicatrix frame {N_p, N_m, N_g}, where the axes are labelled according to the convention for the principal refractive indices $n_p < n_m < n_g$. The N_p-axis parallel to the crystallographic ***b***-axis, which is also the 2-fold symmetry axis (C_2), see Fig. 2(d). The N_g and N_m axes are lying in the orthogonal ***a***-***c*** plane (the mirror plane, *m*) [29,38]. This arrangement of the principal optical directions determines the polarization selection rules for the dopant ions. The angle between the highest refractive index axis, N_g, and the ***c***-axis, is 19.2°, measured outside of the monoclinic angle, and that between the intermediate refractive index axis, N_m, and the ***a***-axis, is 60.0°, within the monoclinic angle [39].

A fragment of the $KGd(WO_4)_2$ structure is presented in Fig. 3 based on the fractional atomic coordinates reported in [37], along with the [Sm|GdO_8], [WO_6], and [KO_{12}] coordination polyhedra. The [Sm|GdO_8] polyhedra are organized in long chains running along the [101] direction. Moreover, two adjacent [WO_6] octahedra sharing O–O edges are forming W_2O_8 units, which are organized as double chains along the crystallographic [001] axis [29]. The host-forming Gd^{3+} ions reside in a single type of sites (Wyckoff: 4*e*, C_2 symmetry) with eight-fold oxygen coordination. The Gd–O interatomic distances are 2.271 Å [37]. The Sm^{3+} dopant ions are replacing the Gd^{3+} host-forming ions thus adopting the same C_2 site symmetry, as their ionic radii are relatively close (R_{Gd} = 1.053 Å and R_{Sm} = 1.079 Å [40]). The shortest Gd–Gd distance is relatively long, 4.070 Å, along the [101] direction. This reduces the cross-talk between the dopant ions leading to a relatively weak concentration quenching of luminescence.

2.2. Characterization methods

Rectangular samples were cut from the as-grown crystal boules with different Sm^{3+} doping levels and oriented in the optical indicatrix frame with all six lateral faces polished, see an example photograph of a 0.8 at.% Sm^{3+}-doped crystal sample in Fig. 2(b). These samples were used for polarized spectral measurements and further tested for laser operation.

The polarized luminescence and μ-Raman spectra were measured using a confocal Raman microscope (inVia Qontor, Renishaw) equipped with a 50× Leica objective, a set of polarizing optics, and an Ar^+ ion laser (λ_{exc} = 488 nm, 514 nm). The spectral resolution was about 1 cm^{-1}.

The absorption spectra were recorded with a spectrophotometer (Cary 5000, Agilent) using a Glan-Taylor prism for measurements with polarized light. The spectral bandwidth (SBW) was 0.1 nm in the visible and 0.4 nm in the near-IR.

A spectrofluorometer (QuantaMaster, Horiba) equipped with a photomultiplier tube was used for studying the luminescence dynamics of Sm^{3+} ions.

3. Results and discussion

3.1. Raman spectra

The polarized Raman spectra of the 0.4 at.% Sm:$KGd(WO_4)_2$ crystal are shown in Fig. 4. The measurements were made in the $\boldsymbol{p}(ij)\bar{\boldsymbol{p}}$ geometry (where *i*, *j* = *m* or *g*), using Porto's notations for polarized Raman spectroscopy [41]). They are well in line with the Raman spectra of other monoclinic double tungstate crystals. Here, we just briefly discuss their interpretation.

The factor group analysis for $KGd(WO_4)_2$ predicts the following set of irreducible representations at the center of the Brillouin zone Γ(***k*** = 0): $17A_g + 19B_g + 17A_u + 19B_u$. The A_g and B_g modes are Raman active (out of them, the optical translational lattice modes are $2A_g + 4B_g$), optical librational lattice modes are $3A_g + 3B_g$) and optical internal modes for the W_2O_8 units are $12A_g + 12B_g$), and the A_u and B_u modes are IR-active [42,43].

The phonons with small energies below 260 cm^{-1} are due to external lattice modes associated with translational motion of the cations of the structure (K^+, Gd^{3+}, and W^{6+}) and rotational motion of [WO_6] groups. The bending modes are found in the intermediate energy range of 290–440 cm^{-1}, while the stretching modes are spread over in the 400–900 cm^{-1} range. The particular feature of monoclinic double tungstates is the appearance of vibrations within the range of 430–750 cm^{-1} region, not present for tungstate crystals with isolated WO_4 tetrahedra, which originate from vibrations of double oxygen bridges. The internal Raman mode with the highest energy at 900 cm^{-1} is assigned as $\nu(W - O)/\nu_1$ and is related to stretching vibrations within the [WO_6] groups [42].

3.2. Optical absorption

Figure 5 shows the absorption spectra of the 0.4 at.% Sm^{3+}:$KGd(WO_4)_2$ crystal in four wavelength intervals between 340 and 3000 nm for the three principal light polarizations, $\boldsymbol{E} \parallel N_p$, N_m and N_g. It is expressed in terms of the absorption cross-sections, $\sigma_{abs} = \alpha_{abs}/N_{Sm}$ (α_{abs} – absorption coefficient).

Sm^{3+} ions in $KGd(WO_4)_2$ exhibit a strong polarization anisotropy of the absorption properties, with more intense absorption for light polarizations $\boldsymbol{E} \parallel N_m$ and $\boldsymbol{E} \parallel N_p$. The absorption transitions occur only from the $^6H_{5/2}$ ground-state, as the next manifold ($^6H_{7/2}$) is located at ~1000 cm^{-1} above and its thermal population at room temperature is negligible. The transitions are assigned according to Carnall *et al.* [44], and *grey labels* indicate transitions to excited-states with nearly zero squared reduced matrix elements $U^{(k)}$ (k = 2, 4, 6) thus almost not contributing to the observed optical absorption.

In the blue spectral range suitable for optical pumping of Sm^{3+} ions for achieving laser emission in the visible, the broad absorption at 430 – 490 nm is due to the spectrally overlapping transitions from the $^6H_{5/2}$ ground-state to the group of closely located ^4G_J, ^4I_J, ^4M_J and ^4F_J manifolds. This spectral range can be readily addressed by commercial blue GaN-based laser diodes. All these transitions are spin-forbidden ($\Delta S \neq 0$) and therefore exhibit relatively low absorption cross-sections on the order of a few 10^{-21} cm^2 as seen in Fig. 5(b). Among them, the $^6H_{5/2} \rightarrow {}^4M_{15/2}$ transition corresponds to the highest absorption cross-section of 0.75×10^{-20} cm^2 at 478.8 nm for light polarization $\boldsymbol{E} \parallel N_m$ and the corresponding absorption bandwidth (full width at half maximum, FWHM) is 2.6 nm. The absorption cross-sections for Sm:$KGd(WO_4)_2$ are higher than those for the Sm:$LiLuF_4$ crystal previously employed in Sm-lasers (σ_{abs} = 0.48×10^{-20} cm^2 at 478.4 nm for π-polarization) [25], which is a typical feature of the low-symmetry double-tungstate host materials.

At shorter wavelengths, in the range between 400 nm and 420 nm shown in Fig. 5(a), an order of magnitude higher absorption cross-sections on the order of few 10^{-20} cm^2 are found owing to the spin-allowed ($\Delta S = 0$) transitions into the higher-lying $^6P_{5/2}$ and $^6P_{3/2}$ manifolds. In particular, for the $^6H_{5/2} \rightarrow {}^6P_{3/2}$ transition, σ_{abs} reaches 7.13×10^{-20} cm^2 at 404.6 nm for light polarized $\boldsymbol{E} \parallel N_m$ with an absorption bandwidth of 2.0 nm. Also in this case, Sm:$LiLuF_4$ exhibits significantly lower absorption, with σ_{abs} of 1.51×10^{-20} cm^2 at 401.0 nm for π-polarized light [25].

3.3. Judd-Ofelt theory

The Judd-Ofelt (J-O) theory was applied to describe the intensities of 4f-4f transitions of Sm^{3+} ions in $KGd(WO_4)_2$ based on the measured polarized absorption spectra. One of the basic assumptions within the standard J-O theory [45,46] is that the ground configuration and the excited configuration of the opposite parity ($4f^5$ and $4f^45d^1$ for Sm^{3+} ions, respectively) are completely degenerated and the excited configuration is located at much higher energies, and its influence on all the manifolds of the ground configuration is identical. According to Dorenbos *et al.*, the $4f^45d^1$ Sm^{3+} configuration has an intermediate energy among other trivalent rare-earth ions and thus its effect may be useful to be considered in a more precise way in particular

in high crystal field depression materials such as double tungstates [10]. Kornienko *et al.* developed a modified Judd-Ofelt (mJ-O) theory accounting for weak configuration interaction [47]. Within this theory, the line strengths of electric-dipole transitions are given by [48]:

$$S_{\mathrm{calc}}^{\mathrm{ED}}(JJ') = \sum_{\mathrm{k}=2,4,6} U^{(\mathrm{k})}\tilde{\Omega}_{\mathrm{k}}\,, \tag{1a}$$

$$\tilde{\Omega}_{\mathrm{k}} = \Omega_{\mathrm{k}}[1 + 2\alpha(E_{\mathrm{J}} + E_{\mathrm{J}'} - 2E_{\mathrm{f}}^{0})]. \tag{1b}$$

According to Eq. (1), the intensity parameters $\tilde{\Omega}_{\mathrm{k}}$ (k = 2, 4, 6) are no longer constant like in the standard J-O theory but linear depending on the energies (denoted by E_{J} and $E_{\mathrm{J}'}$) of the two manifolds involved in the considered J → J' transition, where E_{f}^{0} is the mean energy of the ground configuration ($4f^n$) and the parameter α can be expressed as $1/(2\Delta_{5d})$, where Δ_{5d} is the mean energy separation between the ground ($4f^n$) and excited ($4f^{n-1}5d^1$) configurations. For a higher-lying $4f^{n-1}5d^1$ configuration ($\Delta_{5d} \rightarrow \infty$), one arrives at $\alpha \rightarrow 0$ and $\tilde{\Omega}_{\mathrm{k}}$ become independent of the manifold energy, which yields the standard J-O theory:

$$S_{\mathrm{calc}}^{\mathrm{ED}}(JJ') = \sum_{\mathrm{k}=2,4,6} U^{(\mathrm{k})}\Omega_{\mathrm{k}}, \tag{2a}$$

$$U^{(\mathrm{k})} = \langle (4\mathrm{f}^{\mathrm{n}})SLJ \,||\, U^{\mathrm{k}} \,||\, (4\mathrm{f}^{\mathrm{n}})S'L'J' \rangle^2 . \tag{2b}$$

Note that the energy-independent intensity parameters Ω_k (k = 2, 4, 6) which appear in Eq. (1a) and Eq. 2(a) are not directly comparable.

In the present work, we used both the J-O and mJ-O parametrization schemes to describe the electric-dipole (ED) transitions of Sm^{3+} ions. The contribution of magnetic-dipole (MD) transitions obeying the selection rules $\Delta S = 0$, $\Delta L = 0$, $\Delta J = 0, \pm 1$ were calculated separately within the Russell–Saunders approximation on Sm^{3+} wave functions assuming a free-ion. The full set of reduced squared matrix elements $U^{(k)}$ (k = 2, 4, 6) for transitions in absorption emission was calculated in the present work on wave functions calculated in their turn from the free-ion parameters reported for Sm^{3+} [44]. The refractive index of the crystal was calculated from the Sellmeier equations reported [39].

The experimental absorption oscillator strengths $\langle f_{exp} \rangle$, were calculated as:

$$< f_{exp} > = \frac{m_e c^2}{\pi e^2 N_{Sm} <\lambda>^2} < \Gamma >, \tag{3}$$

with m_e and e being the electron mass and charge, respectively, c representing the speed of light, N_{Sm} being the ion density in the 0.4 at.% Sm-doped crystal (0.25×10^{20} at/cm^3), $\langle\lambda\rangle$ denoting the center of gravity of the absorption band, and $\langle\Gamma\rangle$ being the absorption coefficient integrated over this band corresponding to a particular transition or a group of undistinguishable (spectrally overlapping) transitions. The brackets <..> stand for polarization-averaging, $\langle f_{exp} \rangle = (f_p + f_m + f_g)/3$. The results on $\langle f_{exp} \rangle$ are given in Table 1. A total of N = 11 transitions were analyzed (out of them, 5 transitions had an MD contribution).

The absorption oscillator strengths can be calculated from the corresponding line strengths depending on the set of intensity parameters (Ω_2, Ω_4, Ω_6 for the standard J-O theory and Ω_2, Ω_4, Ω_6 and α for the mJ-O one):

$$f_{\mathrm{calc}}^{\Sigma}(JJ') = \frac{8}{3h(2J+1)\langle\lambda\rangle}\frac{(n^2+2)^2}{9n} S_{\mathrm{calc}}^{\mathrm{ED}}(JJ') + f_{\mathrm{calc}}^{\mathrm{MD}}(JJ'), \tag{4}$$

where h stands for the Planck constant, n is the mean refractive index of the crystal at the average transition wavelength $\langle\lambda\rangle$ and the superscript "Σ" is labelling the total (ED + MD) value. The set of $\langle f_{exp} \rangle$ is fitted using Eq. (4) and Eq. (1) (mJ-O theory) or Eq. (2) (standard J-O theory) yielding the fitting intensity parameters and the set of calculated absorption oscillator strengths, f^{Σ}_{calc}. The set of squared reduced matrix elements $U^{(k)}$ in absorption used for this fitting is listed in Table 2.

As a merit of goodness of the fit, we calculated the root mean square (r.m.s.) deviation between $<f_{exp}>$ and f^{Σ}_{calc} values:

$$\delta_{RMS} = \sqrt{\frac{1}{N-N_{param}}\sum_i (< f^{\Sigma}_{exp} > - < f^{\Sigma}_{calc} >)^2}. \quad (5)$$

In our case, δ_{rms} for the standard and modified J-O theories are rather close, being 0.999 and 1.020, respectively. Another criterion for the choice of the model is the radiative lifetime of the metastable level: the mJ-O theory provided better agreement with the measured intrinsic luminescence lifetime. Thus, it was chosen for further calculations.

The sets of intensity parameters for the two models applied are given in Table 3. For the mJ-O theory, they are Ω_2 = 8.027, Ω_4 = 7.210 and Ω_6 = 2.322 [10^{-20} cm^2] and α = -0.017 [10^{-4} cm]. The parameter Ω_2 strongly depends on the short-range interactions, *i.e.*, the chemical bonding between the rare-earth ions and the surrounding ligands, as well as the local site symmetry. On the contrary, Ω_4 and Ω_6 depend on the long-range interactions, with Ω_6 being influenced by the rigidity of the matrix [49].

Based on the intensity parameters from the mJ-O theory, the probabilities of spontaneous radiative transitions from the $^4G_{5/2}$ metastable state of Sm^{3+}, $A_{JJ'}$, were evaluated:

$$A^{\Sigma}_{\text{calc}}(JJ') = \frac{64\pi^4 e^2}{3h(2J+1)\langle\lambda\rangle^3} n\left(\frac{n^2+2}{3}\right)^2 S^{\text{ED}}_{\text{calc}}(JJ') + A^{\text{MD}}_{\text{calc}}(JJ'). \quad (6)$$

The total probability of radiative spontaneous transitions, A_{tot}, was then calculated as the sum of the individual $A(JJ')$ values for all the possible emission channels. Using this value, the radiative lifetime, τ_{rad}, as well as the luminescence branching ratios, $B(JJ')$, were obtained by:

$$A_{tot} = \sum_{J'} A^{\Sigma}_{calc}(JJ') \text{ and } \tau_{\text{rad}} = \frac{1}{A_{tot}}, \quad (7)$$

$$B(JJ') = \frac{A^{\Sigma}_{calc}(JJ')}{A_{tot}}. \quad (8)$$

The results on the transition intensities of Sm^{3+} ions in emission are given in Table 4. The set of squared reduced matrix elements $U^{(k)}$ in emission used for this calculation is listed in Table 5. The luminescence branching ratios, $B(JJ')$, are valuable to predict the relative intensities of emission for each radiative transition from a given emitting state. The highest $B(JJ')$ of 40.2% corresponds to the $^4G_{5/2} \rightarrow {}^6H_{9/2}$ transition in the red, and the second most intense is found for the $^4G_{5/2} \rightarrow {}^6H_{7/2}$ transition in the orange, with $B(JJ')$ of 33.8%. Note that these two transitions are mainly exploited in visible Sm-lasers.

The calculated radiative lifetime of the $^4G_{5/2}$ state of Sm^{3+} ions in the $KGd(WO_4)_2$ crystal is 734 μs. It is somewhat shorter than that for the disordered 2 at.% Sm:$NaGd(MoO_4)_2$ double molybdate crystal, τ_{rad} = 979 μs [50]. As expected due to the low symmetry of the cation site in $KGd(WO_4)_2$, this radiative lifetime is much shorter than the values calculated previously for fluoride laser host matrices with intrinsically weaker crystal-field strengths, namely τ_{rad} = 4.6 ms for a 2.2 at.% Sm:$LiLuF_4$ crystal [25] and τ_{rad} = 5.4 ms for a 5.0 at.% Sm:K_2GdF_5 crystal [51].

3.4. Stimulated-emission cross-sections

The polarized luminescence spectra of Sm^{3+} ions in the $KGd(WO_4)_2$ crystal measured over a broad spectral range of 540 to 970 nm are shown in Fig. 6. As for absorption, Sm^{3+} ions in this compound exhibit a strong polarization anisotropy of emission properties. The highest luminescence intensity is observed for light polarized along the N_m and N_p optical indicatrix axes. As mentioned above, Sm^{3+} ions provide emissions in the visible (at different colors) and near-IR spectral ranges all originating from the same long-living $^4G_{5/2}$ manifold, with the most intense transition found in the red around 650 nm, corresponding to the $^4G_{5/2} \rightarrow {}^6H_{9/2}$ transition.

The polarized stimulated-emission (SE) cross-section, σ_{SE}, spectra were calculated based on the measured luminescence spectra, and the transition probabilities (*i.e.*, the radiative

lifetime τ_{rad} and luminescence branching ratios $B(JJ')$), using the Füchtbauer-Ladenburg (F-L) formula [52]:

$$\sigma_{SE}^{i}(\lambda) = \frac{\lambda^5}{8\pi c < n >^2 \tau_{rad}} \times \frac{B(JJ')W_i(\lambda)}{\frac{1}{3}\sum_{j=p,m,g}\int \lambda W_j(\lambda)d\lambda}, \quad (9)$$

where $W_i(\lambda)$ is the measured spectral profile of the luminescence, λ is the wavelength of light, $<n>$ is the refractive index of the host crystal at the mean emission wavelength, c is the speed of light and $i = p, m, g$ denotes the polarization state. The principal refractive indices were evaluated using the Sellmeier equations reported in [39].

The polarized σ_{SE} spectra are given in Fig. 7. In line with the measured fluorescence spectra, the highest emission cross-sections in the visible are reached for the $^4G_{5/2} \rightarrow {}^6H_{9/2}$ transition in the red spectral range, with $\sigma_{SE} = 0.55\times10^{-20}$ cm^2 at 649.0 nm for light polarization $\boldsymbol{E} \parallel N_p$, with a FWHM emission bandwidth of 1.4 nm, *cf*. Fig. 7(c), and for the $^4G_{5/2} \rightarrow {}^6H_{7/2}$ transition in the orange, with a the maximum σ_{SE} of 0.39×10^{-20} cm^2 at 610.0 nm for the same polarization with an emission bandwidth of 2.1 nm, see Fig. 7(b), as both these transitions correspond to the highest luminescence branching ratios. The peak emission wavelengths, as well as the corresponding peak SE cross-sections for various transitions of Sm^{3+} ions in $KGd(WO_4)_2$ covering the yellow, orange, red, deep-red and IR spectral ranges are listed in Table 4.

A comparison of the σ_{SE} spectra for the $^4G_{5/2} \rightarrow {}^6H_{9/2}$ transition for two Sm:$KGd(WO_4)_2$ crystals featuring a low doping level (0.8 at.% Sm) and a relatively high concentration (20 at.% Sm) is shown in Fig. 8 for light polarizations $\boldsymbol{E} \parallel N_m$ and $\boldsymbol{E} \parallel N_p$. This comparison allows us to conclude about the effect of Sm^{3+} ions on the modification of the crystal-field when the doping level becomes high. One can observe a variation of the emission spectral profiles for the heavily doped crystal, namely, a slight blue-shift of emission peaks and redistribution of their relative intensity. Heavy Sm doping is expected to induce small modifications of the crystalline structure and local environment of Sm^{3+} ions, as they are larger than the Gd^{3+} ions (R_{Gd} = 1.053 Å and R_{Sm} = 1.079 Å for eight-fold oxygen coordination).

3.5. Luminescence kinetics

The luminescence decay from the $^4G_{5/2}$ state of Sm^{3+} ions was studied for several $KGd(WO_4)_2$ crystals with Sm^{3+} doping levels of 0.4 at.%, 0.8 at.%, and 20 at.%. The orange emission at 602 nm corresponding to the $^4G_{5/2} \rightarrow {}^6H_{7/2}$ transition was monitored and the excitation wavelength was 471 nm (to the $^4I_{11/2}$ state). The decay curves are seen in Fig. 9. For the crystal with the lowest studied doping level of Sm^{3+} (0.4 at.%), the luminescence decay is almost single-exponential, Fig. 9(a). The measured luminescence lifetime τ_{lum} for this crystal is 719 μs being very close to the radiative one (τ_{rad} = 734 μs) calculated using the mJ-O theory. Due to the high energetic gap below the $^4G_{5/2}$ manifold, any multi-phonon decay can be excluded despite the high phonon energies of the host matrix. Indeed, the energy-gap from the $^4G_{5/2}$ level to the next lower-lying state ΔE is about 7400 cm^{-1}, and the maximum phonon energy of $KGd(WO_4)_2$ is 900 cm^{-1}, so that $\Delta E/h\nu_{ph}$ >> 5-6 obeying the "energy-gap" law [53]. On increasing the doping concentration, the luminescence lifetime decreases to 686 μs (for 0.8 at.% Sm) and 154 μs (for 20 at.% Sm, *i.e.* the quantum efficiency is as low as ~21% in the latter case). The luminescence decay curves notably deviate from the single-exponential law. As shown in Fig. 1, several CR processes between neighboring Sm^{3+} ions can be responsible for this self-quenching behaviour [25,54].

The decay curves were thus fitted using the Inokuti-Hirayama (I-H) model for multipolar interactions [55]:

$$\varphi(t) = \exp\left(\frac{-t}{\tau_0} - \Gamma\left(1 - \frac{3}{s}\right) \times \frac{4}{3}\pi R_0^3 N_{Sm}\left(\frac{t}{\tau_0}\right)^{\frac{3}{s}}\right), \quad (10)$$

where τ_0 is the intrinsic lifetime of the $^4G_{5/2}$ emitting state in absence of energy transfer, N_{Sm} is the density of optical centers, R_0 is the critical distance between Sm^{3+} ions for which the energy transfer rate equals the spontaneous decay rate, *s* describes the interaction mechanism between the active ions (with *s* equal to 6, 8 and 10 for dipole-dipole (D-D), dipole-quadrupole (D-Q), and quadrupole-quadrupole (Q-Q) interactions, respectively), and Γ is the Euler's function which is equal to 1.77 (D-D), 1.43 (D-Q) and 1.30 (Q-Q). The best-fit parameters for all three measured luminescence decay curves are as following: for crystals doped with 0.4 at.% and 0.8 at.% Sm^{3+} the intrinsic lifetime τ_0 of 750±25 μs, the critical distance between active ions of R_0 of 7.00±0.50 Å, and the *s* parameter of 6 indicating dipole-dipole interaction. For the crystal doped with 20 at.% Sm^{3+}, the same intrinsic lifetime τ_0 of 750±25 μs, the critical distance R_0 of 8.25±0.03 Å, and the *s* parameter of 8 indicating dipole-quadrupole interaction were taken for fitting the decay curve.

Assuming a uniform ion distribution, the average distance between Sm^{3+} ions inside the $KGd(WO_4)_2$ crystal is given by:

$$R_{av} = \left(\frac{4}{3}\pi N_{Sm}\right)^{\frac{-1}{3}}. \quad (11)$$

For low-doped crystals, we arrive to R_{av} of 21.3 Å and 16.9 Å for 0.4 at.% Sm and 0.8 at.% Sm, respectively, *i.e.,* $R_{av} >> R_0$. In this case, the cross-relaxation among adjacent Sm^{3+} ions is weak. For the heavily-doped crystal (20 at.% Sm), one finds R_{av} = 5.8 Å, so that $R_{av} < R_0$. The decay curve strongly deviates from a single exponential decay, indicating a significant energy transfer between Sm^{3+} ions, resulting in strong luminescence lifetime quenching, which is often observed for Sm^{3+}-doped materials. A strong decrease of the luminescence lifetime of the $^4G_{5/2}$ excited state occurred also for Sm^{3+}:$LiYF_4$ crystals, with τ_{lum} values gradually decreasing from 1.5 ms to 0.6 ms upon increasing the doping level in the range of 0.1 - 10 mol% Sm [56].

The luminescence dynamics studies of Sm^{3+} ions reported so far seem to demonstrate that the interionic interactions between Sm^{3+} ions strongly vary with the doping level, as well as the nature and structure of the host material [54,57,58]. Very different interaction mechanisms have been observed using the I-H model for KYP_4O_{12} [57], $CaWO_4$ [58], Y_2WO_6 [59], and $K_5Li_2LaF_{10}$ crystals [54], phosphate and fluorophosphate glasses [60] for various Sm^{3+} doping levels. Lavin *et al*. studied quadrupole-quadrupole interactions for low-doped fluoroborate glasses [61]. Solarz *et al*. observed variations of the interaction mechanism upon increasing the doping level for $K_5Li_2LaF_{10}$ crystals up to the stoichiometric composition, from dipole-dipole interactions to quadrupole-quadrupole ones [54]. Demesh *et al*. investigated $KY(WO_4)_2$ crystals with low Sm^{3+} doping [24]. Similarly to our study of low-doped crystals, the authors concluded about dipole-dipole interactions (*s* = 6) using the I-H model. The reported best-fitting parameters were relatively close to those obtained in the present work, *i.e*., a critical distance R_0 of 8.4 Å, and an intrinsic lifetime of 780 μs. Several authors suggested that the I-H formalism present some limitations for fitting multipolar interactions of Sm^{3+} ions, as it is not taking into account energy migration processes, the discrete structure of the material, or the distance between the second and third nearest neighbors (namely, $2R_0$ and $3R_0$) [54,57]. Nevertheless, concentration quenching was observed in the majority of Sm^{3+}-doped materials studies, at intermediate to high doping levels.

3.6. Excited-state absorption

As mentioned previously, one of the main challenges for developing visible solid-state lasers based on Sm^{3+} ions is the risk of ESA within the 4f configuration, due to its complex energy-level scheme. ESA is a process when a single atom, ion or molecule is excited from a lower-lying excited-state, in our case the metastable state $^4G_{5/2}$, to a higher-lying one by absorption of a photon [62]. ESA at the laser wavelength can strongly influence the output laser performance, or even prevent lasing, while ESA at the pump wavelength greatly reduces the

pumping efficiency [63]. So far, ESA of samarium ions was studied only for divalent Sm^{2+} ions [64]. Marzahl *et al*. studied visible laser action using Sm^{3+}-doped $LiLuF_4$ and $SrAl_{12}O_{19}$ crystals, and they observed a self-pulsing behavior, which they attributed to ESA at the laser wavelength [18]. Even though no such transitions were detected by the pump-probe ESA measurements in their work, these authors did not exclude the possibility of weak (non-resonant) ESA processes.

In the present work, we estimated the probabilities of transitions in excited-state absorption and stimulated emission originating from the $^4G_{5/2}$ manifold of Sm^{3+} ions, *i.e*. the upper laser level, having an average energy $E(^4G_{5/2})$ of 17790 cm^{-1}. These calculations were performed within the mJ-O theory, and the obtained results are listed in Table 7. In this way, we can evaluate the risk of ESA at the potential laser wavelengths in the orange (the $^4G_{5/2} \rightarrow {}^6H_{7/2}$ transition), red (the $^4G_{5/2} \rightarrow {}^6H_{9/2}$ transition), and deep-red (the $^4G_{5/2} \rightarrow {}^6H_{11/2}$ transition) spectral ranges, for Sm:$KGd(WO_4)_2$. In this table, first, we list the barycenter energies of the terminal manifolds for both the ESA and SE transitions (J → J'), denoted as $E_{J'}$. Then, the transition energy $\Delta E_{JJ'}$ is calculated for both types of processes. Finally, we give the Einstein coefficients B_{calc} for these transitions.

Concerning transitions in the red spectral range, the values of $\Delta E_{JJ'}$ for potential ESA channels (14830 cm^{-1} for $^4G_{5/2} \rightarrow {}^4P_{5/2}$, and 15720 cm^{-1} for $^4G_{5/2} \rightarrow {}^2F_{5/2}$) are not resonant with that for the emission transition $^4G_{5/2} \rightarrow {}^6H_{9/2}$ (15720 cm^{-1}). This indicates a small risk of ESA at this laser wavelength. Recently [19], we obtained laser action with the Sm:$KGd(WO_4)_2$ crystal in the red exhibiting a self-pulsing behavior. A weak ESA process could explain this pulsed regime of operation acting as an artificial “fast” saturable absorber, probably originating from the $^4G_{5/2} \rightarrow {}^2F_{5/2}$ ESA transition, presenting the closest transition energy $\Delta E_{JJ'}$ to that of the laser channel, as well as the highest B_{calc} value. Still, this weak (non-resonant) ESA does not prevent lasing.

On the contrary, there is a strong risk of resonant ESA in the orange and deep-red spectral ranges, with both higher values of B_{calc} and smaller energy mismatch between the transition energies $\Delta E_{JJ'}$ in ESA and SE. In the orange spectral range (the $^4G_{5/2} \rightarrow {}^6H_{7/2}$ transition, $\Delta E_{JJ'}$ = 16530 cm^{-1}), the most probable ESA path is the $^4G_{5/2} \rightarrow {}^4F_{9/2}$ transition, with B_{calc} of 0.859×10^{-17} $m^3s^{-2}J^{-1}$ and $\Delta E_{JJ'}$ = 16450 cm^{-1}. Similarly, in the deep-red (the $^4G_{5/2} \rightarrow {}^6H_{11/2}$ transition, $\Delta E_{JJ'}$ = 14020 cm^{-1}), the most probable ESA paths are the $^4G_{5/2} \rightarrow {}^4G_{11/2}$ and $^4G_{5/2} \rightarrow {}^2K_{15/2}$ transitions, with B_{calc} of 0.906×10^{-17} $m^3s^{-2}J^{-1}$ and 2.037×10^{-17} $m^3s^{-2}J^{-1}$, respectively, and transition energies of 13860 and 13630 cm^{-1}, respectively. These strong and nearly resonant ESA processes might prevent laser action in the orange and deep-red spectral ranges. The possible 4f-4f ESA transitions of Sm^{3+} ions at the potential laser wavelengths are shown in Fig. 10.

Due to the crystal-field interaction, the $^4G_{5/2}$ state of Sm^{3+} ions is split in three closely located Stark sub-levels with the energies of 17601, 17876 and 17885 cm^{-1} in $KGd(WO_4)_2$. We calculated the probabilities of thermal population of these sub-levels, at 300 K and 400 K (accounting for the possible heating of the laser element under optical pumping), and the results are presented in Table 8. As very obviously expected, we observed an increase of the fractional thermal population of the higher-lying Stark sub-levels with increasing temperature, namely from 0.176 to 0.215 for the intermediate one, and from 0.168 to 0.207 for the higher-energy one. Thus, ESA conditions could also be affected by variations in the crystal temperature.

3.7. Laser performance

For the laser experiments, we used a rectangular laser element cut from the 0.8 at.% Sm^{3+}-doped crystal and oriented in the optical indicatrix frame. The laser element had dimensions of 6.00(N_p) × 7.70(N_m) × 8.05(N_g) mm^3. It was oriented for light propagation along the N_g-axis (N_g-cut) due to the good thermo-optical properties offered by this crystal cut [65]. A

photograph of the laser element under UV illumination is given in Fig. 2(b). It was mounted in a Cu-holder and passively cooled.

Two high-brightness pump sources were employed: 2ω-OPSL emitting up to 3.5 W at 479.1 nm (Genesis CX, Coherent) and a 2ω-Ti:sapphire laser (MSquared Lasers, SolsTiS ECD-X) delivering up to 1.5 W at 404.7 nm.

We employed a laser setup which is very similar to one reported in [19], see Fig. 11.

First, we explored laser operation in the red spectral range on the $^4G_{5/2} \rightarrow {}^6H_{9/2}$ transition under pumping with the 2ω-OPSL at 479.1 nm. This wavelength corresponds to a local maximum in the absorption spectrum with a peak absorption cross section of 0.68×10^{-20} cm^2 for light polarized $\boldsymbol{E} \parallel N_m$, see Fig. 5(b). The input-output characteristics of the red Sm^{3+}-laser are shown in Fig. 12(a), and the output characteristics are summarized in Table 9. A maximum true peak output power of 37.8 mW was obtained when using an output coupler transmission of 2.2%, with a corresponding laser threshold of 87 mW and a slope efficiency of 17.6% with respect to the absorbed pump power. For output coupler transmissions between 0.7% and 6.2%, the laser threshold increased from 44 mW to 216 mW at lower slope efficiencies than for T_{OC} = 2.2%.

The input-output characteristics did not show a perfect linear trend close to the laser threshold. No signs of detrimental thermal effects nor thermal fracture of the crystal were observed up to the highest incident pump power of 2.0 W. A weak impact of thermo-optic effects was confirmed by implementing a mechanical chopper to modulate the pump beam and testing various pump duty cycles between 1:2 and 1:10, which did not reveal any significant improvement in the slope efficiency, however, a lower laser threshold resulted in a higher laser peak power.

The laser wavelength of ~649 nm was weakly dependent on the output coupling rate. The laser emission was linearly polarized ($\boldsymbol{E} \parallel N_p$) as expected from the emission spectra shown in Fig. 7(c). The far-field laser mode profiles shown in Fig. 12(b-d) were captured for an output coupling of 4.1% at three different output powers. With increasing the pump power, the laser beam is distorted and becomes elliptic. This behaviour is related to a weak astigmatism of the positive thermal lens in N_g-cut monoclinic double tungstate crystals [65].

This laser results represents an improvement in comparison to the first laser demonstration in this gain material [19] in terms of the output power in the red by a factor of two.

Using the frequency-doubled Ti:sapphire laser at 404.7 nm as pump source to make use of the much higher absorption cross-section of 6.8×10^{-20} cm^2 of the spin-allowed $^6H_{5/2} \rightarrow {}^6P_{3/2}$ transition of Sm^{3+}, see Fig. 5(a). However, no laser action in the red was achieved in this case. This can be explained by possible parity-allowed 4f – 5d ESA at this pump wavelength.

Moreover, we performed laser experiments aiming for the orange transition $^4G_{5/2} \rightarrow {}^6H_{7/2}$ and the deep-red transition $^4G_{5/2} \rightarrow {}^6H_{11/2}$, using both pump sources, but again no laser emission was observed. This is most probably due to strong resonant 4f-4f ESA transitions at the laser wavelengths, as predicted by our calculations using the mJ-O formalism.

Finally, the heavily-doped (20 at.% Sm^{3+}) crystal was investigated for laser operation. No laser action was obtained in the red when pumping by 2ω-OPSL at 479.1 nm, presumably due to the strong concentration quenching of the upper laser level $^4G_{5/2}$ by CR processes as evidenced by the measured luminescence decay curve for this sample, see Fig. 9.

4. Conclusions

By performing a comprehensive polarizatrion-resolved spectroscopic study of samarium (III) doped $KGd(WO_4)_2$ crystals as a representative of the crystal family of monoclinic double tungstates, we conclude that these optically biaxial materials are appealing for the development of blue-pumped low-threshold lasers directly emitting red light. This is because of their attractive

spectroscopic properties, such as (i) high absorption cross-sections for polarized light enabling efficient pumping even for low-doped crystals; (ii) intense and strongly polarized stimulated-emission bands in the red (σ_{SE} is 0.55×10^{-20} cm^2 at 649.0 nm for light polarization $\boldsymbol{E} \parallel N_p$ and the corresponding luminescence branching ratio is 40.2%) leading to linearly polarized laser emission; and (iii) high luminescence quantum yield (~94% for 0.8 at.% Sm^{3+} doping) and relatively weak concentration quenching of luminescence due to the relatively long Gd^{3+} - Gd^{3+} interatomic distances. By employing the modified Judd-Ofelt theory, we were able not only to quantify the transition intensities for Sm^{3+} ions in absorption and emission, but also to analyze the possible role of 4f – 4f excited-state absorption in affecting and even ceasing laser operation in the visible, in the orange, red and deep-red spectral ranges. Indeed, ESA to the higher-lying short-living $^4F_{9/2}$ (in the orange) and $^4G_{11/2}$ and $^2K_{15/2}$ (in the deep red) manifolds is suggested as a limiting factor for laser action in these spectral ranges.

Future studies on Sm^{3+}-doped monoclinic double tungstates should involve the following lines to improve their laser performance and better understand the spectroscopic processes affecting laser transitions:

(i) an experimental study of ESA at the potential pump and laser wavelengths, e.g., by the pump-probe method, is needed, to reveal the predicted 4f – 4f ESA channels and to confirm the existence of possible parity-allowed 4f – 5d ESA transitions within the transparency range of monoclinic double tungstates;

(ii) further optimization of the Sm^{3+} doping level around a few at.% is needed to find an equilibrium between the pump absorption efficiency and luminescence quenching;

(iii) and, finally, the prospects of diode-pumping of Sm:$KGd(WO_4)_2$ crystals should be explored for further power scaling. Note that microchip laser operation is expected in this case as N_g-cut monoclinic double tungstate crystals feature a weakly astigmatic positive thermal lens. The role of ESA in the heat generation in such lasers needs to be clarified.

Acknowledgements

Région Normandie, France (Contrat de plan État-Région (CPER)); Deutsche Forschungsgemeinschaft (458056764); Agence Nationale de la Recherche, France (ANR-22-CE08-0025-01, NOVELA).

References

[1] P.-E. Lecoq de Boisbaudran, Recherches sur le samarium, radical d'une terre nouvelle extraite de la samarskite, C. R. Acad. Sci. Paris 89 (1879) 212-214, https://gallica.bnf.fr/ark:/12148/bpt6k3046j.
[2] C. Kränkel, D.-T. Marzahl, F. Moglia, G. Huber, P. W. Metz, Out of the blue: semiconductor laser pumped visible rare-earth doped lasers, Laser Photonics Rev. 10 (2016) 548–568, doi: 10.1002/lpor.201500290.
[3] S. Duffy, J.-P. R. Wells, H. G. Gallagher, T. P. J. Han, Bridgman growth and laser excitation of $LiYF_4$:Sm^{3+}, J. Cryst. Growth 203 (1999) 405-411, doi: 10.1016/S0022-0248(99)00128-1.
[4] J. Li, J. Yan, D. Wen, W. U. Khan, J. Shi, M. Wu, Q. Su, P. A. Tanner, Advanced red phosphors for white light-emitting diodes, J. Mater. Chem. C 4 (2016) 8611-8623, doi: 10.1039/c6tc02695h.
[5] A. Raja, R. Nagaraj, K. Ramachandran, V. Sivasubramani, G. Annadurai, D. Joseph Daniel, P. Ramasamy, A facile synthesis, structural and triple-luminescence properties of a novel fluoroperovskite $RbCaF_3$:Sm^{3+} phosphor for radiation dosimetry and orange-red LED applications, Mater. Sci. Eng. B. 255 (2020) 114531, doi: 10.1016/j.mseb.2020.114531.
[6] P. Leblans, D. Vandenbroucke, P. Willems, Storage phosphors for medical imaging, Materials 4 (2011) 1034-1086, doi: 10.3390/ma4061034.
[7] W. Liu, Q. Zhang, D. Sun, J. Luo, C. Gu, H. Jiang, S. Yin, Crystal growth and spectral properties of Sm:GGG crystal, J. Cryst. Growth 331 (2011) 83-86, doi: 10.1016/j.jcrysgro.2011.07.023.
[8] W. Zhou, Q. Zhang, J. Xiao, J. Q. Luo, W. Liu, H. Jiang, S. Yin, Sm^{3+}-doped (Ca, Mg, Zr)GGG crystal: A potential reddish-orange laser crystal, J. Alloys Compd 491 (2010) 618-622, doi: 10.1016/j.jallcom.2009.11.018.

[9] A. Lupei, V. Lupei, C. Gheorghe, Electronic structure of Sm^{3+} ions in YAG and cubic sesquioxide ceramics, Opt. Mater 36 (2013) 419-424, doi: 10.1016/j.optmat.2013.10.004.
[10] P. Dorenbos, The $4f^n \leftrightarrow 4f^{n-1}5d$ transitions of the trivalent lanthanides in halogenides and chalcogenides, J. Lumin. 91 (2000) 91-106, doi: 10.1016/S0022-2313(00)00197-6.
[11] P. P. Sorokin, M. J. Stevenson, Solid-state optical maser using divalent samarium in calcium fluoride, IBM J. Res. Dev. 5 (1961) 56-58, doi: 10.1147/rd.51.0056.
[12] B. N. Kazakov, M. S. Orlov, M. V. Petrov, A. L. Stolov, A. M. Tkachuk, Induced emission of Sm^{3+} ions in the visible region of the spectrum, Opt. Spectrosc. 47 (1979) 676-677.
[13] M. C. Farries, P. R. Morkel, J. E. Townsend, Samarium^{3+}-doped glass laser operating at 651 nm, Electron. Lett. 24 (1988) 709-711, doi: 10.1049/el:19880479.
[14] M. C. Farries, P. R. Morkel, J. E. Townsend, Spectroscopic and lasing characteristics of samarium doped glass fibre, IEE Proc. J. 137 (1990) 318-322, doi: 10.1049/ip-j.1990.0054.
[15] H. P. Jenssen, Visible (orange) laser emission from Sm doped $LiTbF_4$, ASSL Tech. Dig. ME2-1/73 (1995).
[16] S. Nakamura, M. Senoh, S.-I. Nagahama, N. Iwasa, T. Yamada, T. Matsushita, H. Kiyoku, Y. Sugimoto, InGaN-based multi-quantum-well-structure laser diodes, Jpn. J. Appl. Phys. 35 (1996) L74-L76, doi: 10.1143/JJAP.35.L74.
[17] M. Kuznetsov, F. Hakimi, R. Sprague, A. Mooradian, High-power (>0.5-W CW) diode-pumped vertical-external-cavity surface-emitting semiconductor lasers with circular TEM_{00} beams, IEEE Photonics Technol. Lett. 9 (1997) 1063-1065, doi: 10.1109/68.605500.
[18] D.-T. Marzahl, P. W. Metz, C. Kränkel, G. Huber, Spectroscopy and laser operation of Sm^{3+}-doped lithium lutetium tetrafluoride ($LiLuF_4$) and strontium hexaaluminate ($SrAl_{12}O_{19}$), Opt. Express 23 (2015) 21118-21127, doi: 10.1364/OE.23.021118.
[19] A. Baillard, P. Loiko, D. Rytz, S. Schwung, M. Fromager, A. Braud, P. Camy, Red Sm:$KGd(WO_4)_2$ laser at 649 nm, Opt. Lett. 48 (2023) 4721-4724, doi: 10.1364/OL.498100.
[20] C. L. Goh, The role of lasers and light devices for the treatment of melasma, in Melasma and vitiligo in brown skin, (2017) 143-157, doi: 10.1007/978-81-322-3664-1_16.
[21] L. J. Walsh, The current status of laser applications in dentistry, Aust. Dent. J. 48 (2003), doi: 10.1111/j.1834-7819.2003.tb00025.x.
[22] J. Senarathna, A. Rege, N. Li, N. V. Thakor, Laser speckle contrast imaging: theory, instrumentation and applications, IEEE Rev. Biomed. Eng. 6 (2013) 99-110, doi: 10.1109/RBME.2013.2243140.
[23] K. Johnson, M. Hibbs-Brenner, W. Hogan, M. Dummer, Advances in red VCSEL technology, Adv. Opt. Technol. (2012), doi: 10.1155/2012/569379.
[24] M. P. Demesh, O. P. Dernovich, N. V. Gusakova, A. S. Yasukevich, A. A. Kornienko, E. B. Dunina, L. A. Fomicheva, A. A. Pavlyuk, N. V. Kuleshov, Growth and spectroscopic properties of Sm^{3+}:$KY(WO_4)_2$ crystal, Opt. Mater. 75 (2018) 821-826, doi: 10.1016/j.optmat.2017.12.001.
[25] G. Q. Wang, X. H. Gong, Y. F. Lin, Y. J. Chen, J. H. Huang, Z. D. Luo, Y. D. Huang, Polarized spectral properties of Sm^{3+}:$LiLuF_4$ crystal for visible laser application, Opt. Mater. 37 (2014) 229-234, doi: 10.1016/j.optmat.2014.05.033.
[26] G. Bolognesi, D. Parisi, D. Calonico, G. A. Costanzo, F. Levi, P. W. Metz, C. Kränkel, G. Huber, M. Tonelli, Yellow laser performance of Dy^{3+} in co-doped Dy,Tb:$LiLuF_4$, Opt. Lett. 39 (2014) 6628-6631, doi: 10.1364/OL.39.006628.
[27] A. Remky, A. E. Elsner, Blue on yellow perimetry with scanning laser ophthalmoscopy in patients with age related macular disease, Br. J. Ophthalmol. 89 (2005) 464-469, doi: 10.1136/bjo.2004.050260.
[28] Y. Feng, L. R. Taylor, D. Bonaccini Calia, 25 W Raman-fiber-amplifier-based 589 nm laser for laser guide star, Opt. Express 17 (2009), doi: 10.1364/OE.17.019021.
[29] V. Petrov, M. C. Pujol, X. Mateos, Ò. Silvestre, S. Rivier, M. Aguiló, R. M. Solé, J. Liu, U. Griebner, F. Díaz, Growth and properties of $KLu(WO_4)_2$, and novel ytterbium and thulium lasers based on this monoclinic crystalline host, Laser Photonics Rev. 1 (2007) 179-212, doi: 10.1002/lpor.200710010.
[30] A. Kaminskii, U. Hömmerich, D. Temple, J. T. Seo, K.-I. Ueda, S. Bagayev, A. Pavlyuk, Visible laser action of Dy^{3+} ions in monoclinic $KY(WO_4)_2$ and $KGd(WO_4)_2$ crystals under Xe-flashlamp pumping, Jpn. J. Appl. Phys. 39 (2000) L208-L211, doi: 10.1143/JJAP.39.L208.

[31] V. I. Dashkevich, S. N. Bagayev, V. A. Orlovich, A. A. Bui, P. A. Loiko, K. V. Yumashev, A. S. Yasukevich, N. V. Kuleshov, S. M. Vatnik, A. A. Pavlyuk, Red Eu,Yb:$KY(WO_4)_2$ laser at ~702 nm, Laser Phys. Lett. 12 (2015) 085001, doi: 10.1088/1612-2011/12/8/085001.
[32] P. A. Loiko, V. I. Dashkevich, S. N. Bagaev, V. A. Orlovich, A. S. Yasukevich, K. V. Yumashev, N. V. Kuleshov, E. B. Dunina, A. A. Kornienko, S. M. Vatnik, Spectroscopic characterization and pulsed laser operation of Eu^{3+}-$KGd(WO_4)_2$ crystal, Laser Phys. 23 (2013) 105811, doi: 10.1088/1054-660X/23/10/105811.
[33] P. Loiko, D. Rytz, S. Schwung, P. Pues, T. Justel, J.-L. Doualan, P. Camy, Watt-level europium laser at 703 nm, Opt. Lett. 46 (2021) 2702-2705, doi: 10.1364/OL.428706.
[34] A. A. Kaminskii, J. B. Gruber, S. N. Bagaev, K.-I. Ueda, U. Hömmerich, J. T. Seo, D. Temple, B. Zandi, A. A. Kornienko, E. B. Dunina, A. A. Pavlyuk, R. F. Klevtsova, F. A. Kuznetsov, Optical spectroscopy and visible stimulated emission of Dy^{3+} ions in monoclinic α−$KY(WO_4)_2$ and α−$KGd(WO_4)_2$ crystals, Phys. Rev. B 65 (2002) 125108(1)-125108(29), doi: 10.1103/PhysRevB.65.125108.
[35] D. Rytz, K. Dupré, A. Gross, C. Liebald, M. Peltz, P. Pues, S. Schwung, V. Wesemann, Crystal growth of rare-earth doped and rare-earth containing materials, Rare Earth Chemistry (2020) 425-438, doi: 10.1515/9783110654929-027.
[36] A. A. Pavlyuk, Y. V. Vasiliev, L. Y. Kharchenko, F. A. Kuznetsov, Low thermal gradient technique and method for large oxide crystals growth from melt and flux, Proc. Asia Pac. Soc. Adv. Mat. (1992) 26-29.
[37] M. C. Pujol, M. Rico, C.do, R. M. Sole, V. Nikolov, X. Solans, M. Aguiló, F. Díaz, Crystalline structure and optical spectroscopy of Er^{3+}-doped $KGd(WO_4)_2$ single crystals, Appl. Phys. B 68 (1999) 187-197, doi: 10.1007/s003400050605.
[38] P. A. Loiko, V. I. Dashkevich, S. N. Bagaev, V. A. Orlovich, A. S. Yasukevich, K. V. Yumashev, N. V. Kuleshov, E. B. Dunina, A. A. Kornienko, S. M. Vatnik, A. A. Pavlyuk, Spectroscopic and photoluminescence characterization of Eu^{3+}-doped monoclinic $KY(WO_4)_2$ crystal, J. Lumin. 153 (2014) 221-226, doi: 10.1016/j.jlumin.2014.03.037.
[39] P. Loiko, P. Segonds, P. L. Inácio, A. Peña, J. Debray, D. Rytz, V. Filippov, K. Yumashev, M. C. Pujol, X. Mateos, M. Aguiló, F. Díaz, M. Eichhorn, B. Boulanger, Refined orientation of the optical axes as a function of wavelength in three monoclinic double tungstate crystals $KRE(WO_4)_2$ (RE = Gd, Y or Lu), Opt. Mater. Express 6 (2016) 2984-2990, doi: 10.1364/OME.6.002984.
[40] R. D. Shannon, Revised effective ionic radii and systematic studies of interatomic distances in halides and chalcogenides, Acta Cryst. A 32 (1976) 751-767, doi: 10.1107/S0567739476001551.
[41] T. C. Damen, S. P. S. Porto, B. Tell, Raman effect in zinc oxide, Phys. Rev. 142 (1966) 570–574, doi: 10.1103/PhysRev.142.570.
[42] L. Macalik, P. J. Dereń, J. Hanuza, W. Stręk, A. A. Demidovich, A. N. Kuzmin, Effect of random distribution and molecular interactions on optical properties of Er^{3+} dopant in $KY(WO_4)_2$ and Ho^{3+} in $KYb(WO_4)_2$, J. Mol. Struct. 450 (1998) 179-192, doi: 10.1016/S0022-2860(98)00427-X.
[43] L. Macalik, J. Hanuza, and A. A. Kaminskii, Polarized infrared and Raman spectra of $KGd(WO_4)_2$ and their interpretation based on normal coordinate analysis, J. Raman Spectrosc. 33 (2002) 92-103, doi: 10.1002/jrs.829.
[44] W. T. Carnall, P. R. Fields, K. Rajnak, Electronic Energy Levels in the Trivalent Lanthanide Aquo Ions. I. Pr^{3+}, Nd^{3+}, Pm^{3+}, Sm^{3+}, Dy^{3+}, Ho^{3+}, Er^{3+}, and Tm^{3+}, J. Chem. Phys. 49 (1968) 4424-4442, doi: 10.1063/1.1669893.
[45] B. R. Judd, Optical absorption intensities of rare-earth ions, Phys. Rev. 127 (1962) 750-761, doi: 10.1103/PhysRev.127.750.
[46] G. S. Ofelt, Intensities of crystal spectra of rare-earth ions, J. Chem. Phys. 37 (1962) 511-520, doi: 10.1063/1.1701366.
[47] A. A. Kornienko, A. A. Kaminskii, E. B. Dunina, Dependence of the line strength of f-f transitions on the manifold energy. II. Analysis of Pr^{3+} in $KPrP_4O_{12}$, Phys. Status Solidi B 157 (1990) 267-273, doi: 10.1002/pssb.2221570127.
[48] P. Loiko, A. Volokitina, X. Mateos, E. Dunina, A. Kornienko, E. Vilejshikova, M. Aguiló, F. Díaz, Spectroscopy of Tb^{3+} ions in monoclinic $KLu(WO_4)_2$ crystal application of an intermediate configuration interaction theory, Opt. Mater. 78 (2018) 495-501, doi: 10.1016/j.optmat.2018.03.014.

[49] C. K. Jorgensen, R. Reisfeld, Judd-Ofelt parameters and chemical bonding, J. Less Common. Met. 93 (1983) 107-112, doi: 10.1016/0022-5088(83)90454-X.
[50] J. Huang, J Huang, Y. Lin, X. Gong, Y. Chen, Z. Luo, Y. Huang, Spectroscopic properties of Sm^{3+}-doped $NaGd(MoO_4)_2$ crystal for visible laser application, J. Lumin. 187 (2017) 235-239, doi: 10.1016/j.jlumin.2016.11.078.
[51] P. V. Do, V. P. Tuyen, V. X. Quang, N. M. Khaidukov, N. TrongThanh, B. Sengthong, B. T. Huy, Energy transfer phenomena and Judd-Ofelt analysis on Sm^{3+} ions in K_2GdF_5 crystal, J. Lumin. 179 (2016) 93-99, doi: 10.1016/j.jlumin.2016.06.051.
[52] B. F. Aull, H. P. Jenssen, Vibronic interactions in Nd:YAG resulting in nonreciprocity of absorption and stimulated emission cross sections, IEEE J. Quantum Electron. 18 (1982) 925-930, doi: 10.1109/JQE.1982.1071611.
[53] M. J. Weber, Probabilities for radiative and nonradiative decay of Er^{3+} in LaF_3, Phys. Rev. 157 (1967) 262, doi: 10.1103/PhysRev.157.262.
[54] P. Solarz, W. Ryba-Romanowski, Luminescence and energy transfer processes of Sm^{3+} in $K_5Li_2LaF_{10}:Sm^{3+}$−$K_5Li_2SmF_{10}$ single crystals, Phys. Rev. B 72 (2005) 075105(1)-075105(8), doi: 10.1103/PhysRevB.72.075105.
[55] M. Inokuti, F. Hirayama, Influence of energy transfer by the exchange mechanism on donor luminescence, J. Chem. Phys. 43 (1965) 1978-1989, doi: 10.1063/1.1697063.
[56] M. Yamaga, H. Uno, S.-I. Tsuda, J.-P. R. Wells, T. P. J. Han, Resonant energy transfer and cross relaxation between Sm^{3+} ions in $LiYF_4$ crystals, J. Lumin. 132 (2012) 1608-1617, doi: 10.1016/j.jlumin.2012.01.028.
[57] M. Malinowski, B. Jacquier, G. Boulon, W. Wolinski, Fluorescence quenching in Sm^{3+} doped KYP_4O_{12} crystals, J. Lumin. 39 (1988) 301-311, doi: 10.1016/0022-2313(88)90011-7.
[58] C. Hsu, R. C. Powell, Dye laser spectroscopy of trivalent samarium in calcium tungstate crystals, J. Phys. C: Solid State Phys. 9 (1976) 2467-2480, doi: 10.1088/0022-3719/9/12/028.
[59] D. Espinoza, N. L. Allan, R. Castillo, S. Conejeros, I. Brito, I. R. Martin, P. Alemany, J. Llanos, Energy transfer, structural and luminescent properties of the color tunable phosphor $Y_2WO_6:Sm^{3+}$, J. Alloys Compd. 835 (2020) 155381, doi: 10.1016/j.jallcom.2020.155381.
[60] V. Venkatramu, P. Babu, C. K. Jayasankar, T. Tröster, W. Sievers, G. Wortmann, Optical spectroscopy of Sm^{3+} ions in phosphate and fluorophosphate glasses, Opt. Mater. 29 (2007) 1429-1439, doi: 10.1016/j.optmat.2006.06.011.
[61] V. Lavín, I. R. Martín, C. K. Jayasankar, T. Tröster, Pressure-induced energy transfer processes between Sm^{3+} ions in lithium fluoroborate glasses, Phys. Rev. B 66 (2002) 064207(1)-064207(7), doi: 10.1103/PhysRevB.66.064207.
[62] L. Guillemot, P. Loiko, J.-L. Doualan, A. Braud, P. Camy, Excited-state absorption in thulium-doped materials in the near-infrared, Opt. Express 30 (2022) 31669-31684, doi: 10.1364/OE.460176.
[63] J. Koetke, G. Huber, Infrared excited-state absorption and stimulated-emission cross sections of Er^{3+}-doped crystals, Appl. Phys. B 61 (1995) 151-158, doi: 10.1007/BF01090936.
[64] J. K. Lawson, Stephen A. Payne, Excited-state absorption spectra and gain measurements of $CaF_2:Sm^{2+}$, J. Opt. Soc. Am. B 8 (1991) 1404-1411 doi: 10.1364/JOSAB.8.001404.
[65] M. S. Gaponenko, P. A. Loiko, N. V. Gusakova, K. V. Yumashev, N. V. Kuleshov, A. A. Pavlyuk, Thermal lensing and microchip laser performance of Ng-cut Tm^{3+}-$KY(WO_4)_2$ crystal, Appl. Phys. B 108 (2012) 603-607, doi: 10.1007/s00340-012-5111-9.

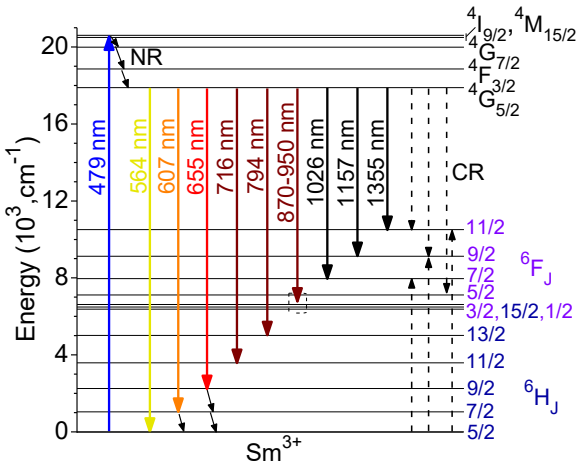

Figure 1. Energy-level scheme of Sm^{3+} ion up to 21000 cm^{-1}. *Arrows* – transitions in absorption and emission, *dashed lines* –cross-relaxation (CR) processes, NR – non-radiative multiphonon relaxation.

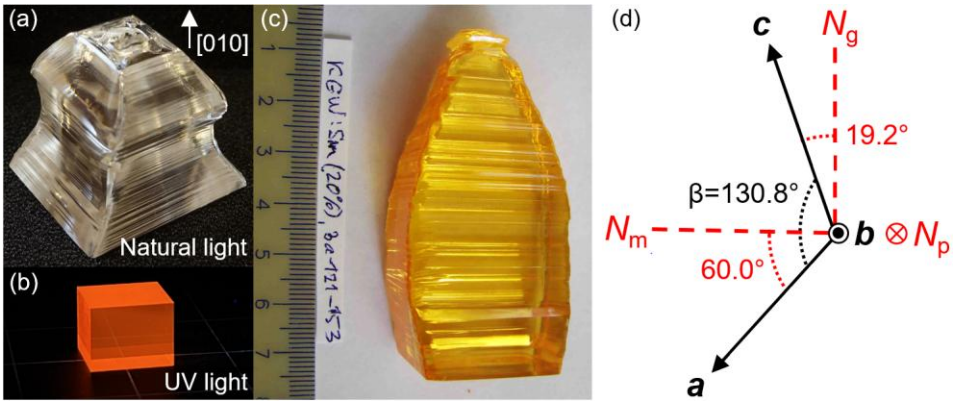

Figure 2. (a-c) Photographs of Sm:$KGd(WO_4)_2$ single crystals, the growth direction is along the [010] axis: (a,b) 0.8 at.% Sm^{3+} doping: (a) an as-grown crystal in natural light, (b) polished laser element under UV illumination; (c) 20 at.% Sm^{3+} doping, an as-grown crystal in natural light; (d) orientation of the optical indicatrix axes {N_p, N_m, N_g} with respect to the crystallographic axes {***a***, ***b***, ***c***}, with the C_2 symmetry axis parallel to the ***b***-axis.

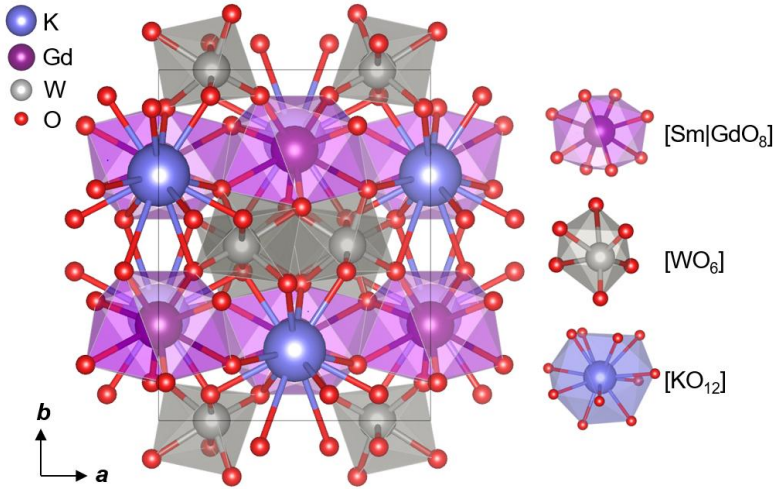

Figure 3. Crystalline structure of monoclinic Sm:KGd$(WO_4)_2$ (sp. gr. *C*2/*c*): (*left*) a fragment of structure within a single unit-cell (*black lines*) in projection on the ***a*-*b*** crystallographic plane, (*right*) the coordination polyhedra [Sm|GdO_8], [WO_6], and [KO_{12}].

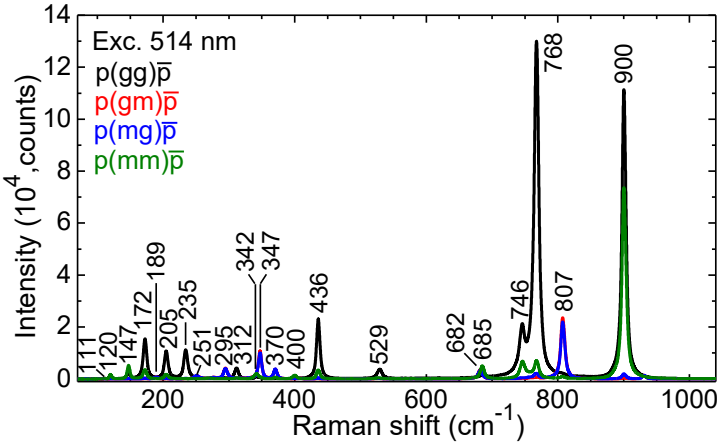

Figure 4. Polarized Raman spectra of the 0.4 at.% Sm:KGd(WO$_4$)$_2$ crystal in the $\boldsymbol{p}(ij)\overline{\boldsymbol{p}}$ geometry (i, j = m, g). Porto's notations are used. λ_{exc} = 514 nm. *Numbers* – Raman frequencies in cm^{-1}.

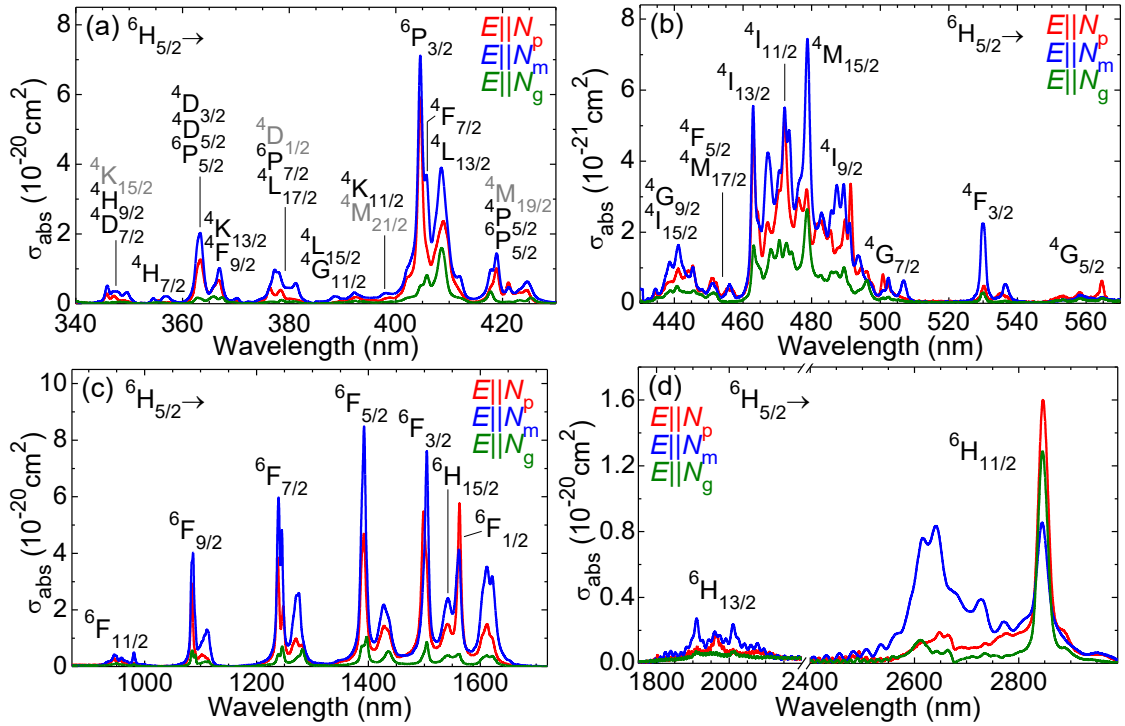

Figure 5. (a-d) Polarized absorption cross-section, σ_{abs}, spectra for Sm^{3+} ions in the 0.4 at.% Sm:KGd(WO$_4$)$_2$ crystal for light polarizations $\boldsymbol{E}$ || N_p, N_m and N_g. The transitions were assigned according to [48], with *grey labels* indicating transitions to excited-states with nearly zero squared reduced matrix elements $U^{(k)}$ (k = 2, 4, 6).

Table 1. Measured and calculated absorption oscillator strengths of Sm^{3+} ions in the 0.4 at.% Sm:$KGd(WO_4)_2$ crystal: E_J – energy of the "center of gravity" of the absorption band, $\langle\Gamma\rangle$ – integrated absorption coefficient, $\langle f_{exp}\rangle$ and f^{Σ}_{calc} – experimental (polarization-averaged) and calculated absorption oscillator strengths, respectively, ED and MD – electric-dipole and magnetic-dipole contributions, respectively.

Transition $^6H_{5/2}\rightarrow{}^{2S+1}L_J$	E_J, cm^{-1}	$\langle\Gamma\rangle$, $cm^{-1}*nm$	$\langle f_{exp}\rangle$, 10^6	f^{Σ}_{calc} (J-O), 10^6	f^{Σ}_{calc} (mJ-O), 10^6
$^6F_{1/2}{}^6H_{15/2}+$ $^6F_{3/2}+{}^6F_{5/2}$	6652.5	359.83	18.144	$16.969^{ED}+$ 0.002^{MD}	$17.534^{ED}+$ 0.002^{MD}
$^6F_{7/2}$	7983.1	87.570	6.271	6.870^{ED}	7.125^{ED}
$^6F_{9/2}$	9083.3	40.763	3.850	3.649^{ED}	3.738^{ED}
$^6F_{11/2}$	10350	14.556	1.803	0.553^{ED}	0.562^{ED}
$^4G_{5/2}$	17727	0.597	0.215	$0.092^{ED}+$ 0.036^{MD}	$0.093^{ED}+$ 0.036^{MD}
$^4F_{3/2}$	18756	0.424	0.169	$0.020^{ED}+$ 0.001^{MD}	$0.020^{ED}+$ 0.001^{MD}
$^4G_{7/2}+{}^4I_{9/2}+{}^4M_{15/2}$ $+{}^4I_{11/2}+{}^4I_{13/2}$	20975	9.060	4.502	$2.127^{ED}+$ 0.001^{MD}	$2.106^{ED}+$ 0.001^{MD}
$^4F_{5/2}+{}^4M_{17/2}+$ $^4G_{9/2}+{}^4I_{15/2}$	22512	1.876	1.070	$0.338^{ED}+$ 0.009^{MD}	$0.334^{ED}+$ 0.009^{MD}
$^6P_{5/2}+{}^4M_{19/2}+$	23750	4.431	17.984	17.568^{ED}	17.601^{ED}
$^4L_{13/2}+{}^4G_{7/2}$	24672	20.946			
$^6P_{3/2}+{}^4K_{11/2}+{}^4M_{21/2}+$ $^4L_{15/2}+{}^4G_{11/2}$	25603	1.144			
$^4D_{1/2}+{}^4L_{17/2}+{}^6P_{7/2}+{}^4K_{13/2}+$	26416	2.234	6.040	6.374^{ED}	6.282^{ED}
$^4F_{9/2}+{}^4D_{3/2}+{}^6P_{5/2}$	27347	5.040			
$^4K_{15/2}+{}^4H_{9/2}+{}^6P_{7/2}$	28782	1.781	1.672	1.294^{ED}	1.247^{ED}
r.m.s. deviation				*0.999*	*1.020*

Table 2. Squared reduced matrix elements for absorption transitions from the fundamental level $^6H_{5/2}$ of Sm^{3+} ions.

Transition $^6H_{5/2} \rightarrow {}^{2S+1}L_J$	Energy E, cm^{-1}	$\|U^{(2)}\|^2$	$\|U^{(4)}\|^2$	$\|U^{(6)}\|^2$
$^6H_{5/2}$	0	0.3879	0.0568	0.0000
$^6H_{7/2}$	1038	0.2061	0.1960	0.0954
$^6H_{9/2}$	2253	0.0256	0.1394	0.3268
$^6H_{11/2}$	3592	0.0000	0.0240	0.2649
$^6H_{13/2}$	5014	0.0000	0.0007	0.0659
$^6F_{1/2}$	6376	0.1939	0.0000	0.0000
$^6H_{15/2}$	6485	0.0000	0.0000	0.0044
$^6F_{3/2}$	6620	0.1444	0.1364	0.0000
$^6F_{5/2}$	7112	0.0332	0.2841	0.0000
$^6F_{7/2}$	7960	0.0020	0.1430	0.4299
$^6F_{9/2}$	9121	0.0000	0.0207	0.3412
$^6F_{11/2}$	10506	0.0000	0.0006	0.0515
$^4G_{5/2}$	17889	0.0002	0.0007	0.0000
$^4F_{3/2}$	18853	0.0003	0.0000	0.0000
$^4G_{7/2}$	19992	0.0004	0.0019	0.0025
$^4I_{9/2}$	20491	0.0023	0.0005	0.0015
$^4M_{15/2}$	20604	0.0000	0.0000	0.0329
$^4I_{11/2}$	21071	0.0000	0.0000	0.0110
$^4I_{13/2}$	21624	0.0000	0.0030	0.0220
$^4F_{5/2}$	22090	0.0004	0.0001	0.0000
$^4M_{17/2}$	22354	0.0000	0.0000	0.0053
$^4G_{9/2}$	22696	0.0001	0.0010	0.0028
$^4I_{15/2}$	22952	0.0000	0.0000	0.0005
$^4M_{19/2}$	23890	0.0000	0.0000	0.0000
$^2F_{5/2}$	24042	0.0000	0.0269	0.0000
$^4L_{13/2}$	24522	0.0000	0.0081	0.0091
$^4F_{7/2}$	24783	0.0002	0.0012	0.0004
$^6P_{3/2}$	24913	0.0000	0.1705	0.0000
$^4K_{11/2}$	25189	0.0000	0.0004	0.0027
$^4M_{21/2}$	25216	0.0000	0.0000	0.0000
$^4L_{15/2}$	25612	0.0000	0.0000	0.0054
$^4G_{11/2}$	25724	0.0000	0.0001	0.0010
$^4D_{1/2}$	26593	0.0001	0.0000	0.0000
$^6P_{7/2}$	26595	0.0000	0.0016	0.0772
$^4L_{17/2}$	26734	0.0000	0.0000	0.0002
$^4K_{13/2}$	26971	0.0000	0.0004	0.0015
$^4F_{9/2}$	27237	0.0000	0.0004	0.0000
$^6P_{5/2}$	27684	0.0000	0.0165	0.0000
$^4D_{3/2}$	27712	0.0001	0.0235	0.0000
$^4H_{7/2}$	28410	0.0013	0.0007	0.0000
$^4K_{15/2}$	28739	0.0000	0.0000	0.0001
$^4H_{9/2}$	29003	0.0001	0.0002	0.0008

Table 3. The intensity parameters of Sm^{3+} ions in the $KGd(WO_4)_2$ crystal.

Parameter	J-O theory	mJ-O theory
Ω_2, 10^{-20} cm^2	9.714	8.027
Ω_4, 10^{-20} cm^2	8.343	7.210
Ω_6, 10^{-20} cm^2	2.763	2.322
α, 10^{-4} cm		-0.017

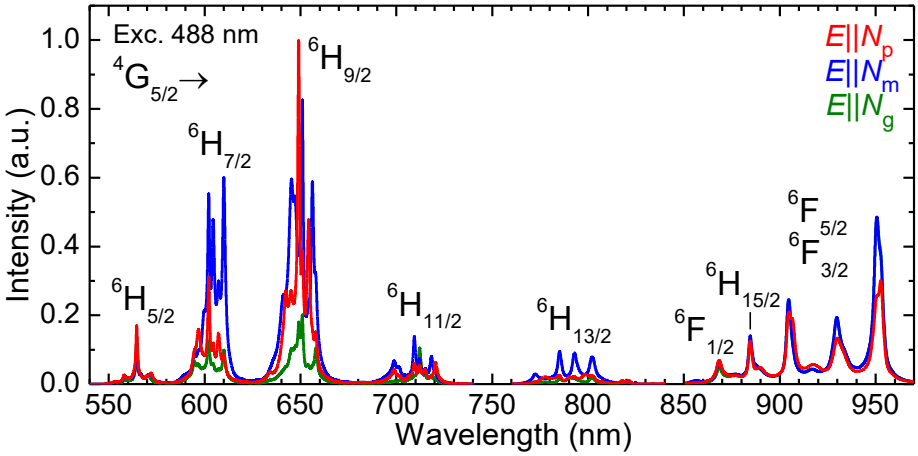

Figure 6. Polarized luminescence spectra of Sm^{3+} ions in the 0.8 at.% Sm:$KGd(WO_4)_2$ crystal in the visible spectral range, with emissions originating from the $^4G_{5/2}$ metastable state and terminating at the ^6H_J and ^6F_J lower-lying manifolds. Light polarizations are $\boldsymbol{E} \parallel N_p$, N_m and N_g. λ_{exc} = 488 nm.

Table 4. The calculated probabilities of spontaneous radiative transitions of Sm^{3+} ions in the $KGd(WO_4)_2$ crystal (the mJ-O model): λ_{em} – peak emission wavelengths for all the possible transitions originating from the $^4G_{5/2}$ metastable state, *A(JJ')* – probabilities of spontaneous radiative transitions (ED + MD), *B(JJ')* – luminescence branching ratios, A_{tot} – total probability of radiative spontaneous transitions, τ_{rad} – radiative lifetime of the $^4G_{5/2}$ state.

$^4G_{5/2}\rightarrow{}^{2S+1}L_J$	λ_{em}, nm	*A(JJ')*, s^{-1}	*B(JJ')*, %	A_{tot}, s^{-1}	τ_{rad}, μs
$^6H_{5/2}$	564.1	$49.93^{ED}+31.27^{MD}$	6.0	1362.5	734.0
$^6H_{7/2}$	607.2	$434.46^{ED}+25.54^{MD}$	33.8		
$^6H_{9/2}$	655.0	548.18^{ED}	40.2		
$^6H_{11/2}$	716.3	114.1^{ED}	8.4		
$^6H_{13/2}$	794.2	12.82^{ED}	0.9		
$^6F_{1/2}+{}^6H_{15/2}+$ $+{}^6F_{3/2}+{}^6F_{5/2}$	903.0	$104.26^{ED}+16.75^{MD}$	8.9		
$^6F_{7/2}$	1026.3	$12.18^{ED}+1.74^{MD}$	1.0		
$^6F_{9/2}$	1156.9	10.59^{ED}	0.8		
$^6F_{11/2}$	1355.6	0.66^{ED}	0.05		

Table 5. The squared reduced matrix elements for transitions in emission from the $^4G_{5/2}$ level of Sm^{3+} ions to the lower-lying levels.

Transition $^4G_{5/2} \rightarrow {}^{2S+1}L_J$	Energy E, cm^{-1}	$\|U^{(2)}\|^2$	$\|U^{(4)}\|^2$	$\|U^{(6)}\|^2$
$^6F_{11/2}$	7383	0.0000	0.0001	0.0004
$^6F_{9/2}$	8768	0.0015	0.0002	0.0003
$^6F_{7/2}$	9929	0.0001	0.0015	0.0001
$^6F_{5/2}$	10777	0.0059	0.0011	0.0000
$^6F_{3/2}$	11269	0.0010	0.0001	0.0000
$^6H_{15/2}$	11404	0.0000	0.0000	0.0001
$^6F_{1/2}$	11513	0.0010	0.0000	0.0000
$^6H_{13/2}$	12875	0.0000	0.0001	0.0019
$^6H_{11/2}$	14297	0.0000	0.0043	0.0016
$^6H_{9/2}$	15636	0.0095	0.0062	0.0018
$^6H_{7/2}$	16851	0.0000	0.0084	0.0072
$^6H_{5/2}$	17889	0.0002	0.0007	0.0000

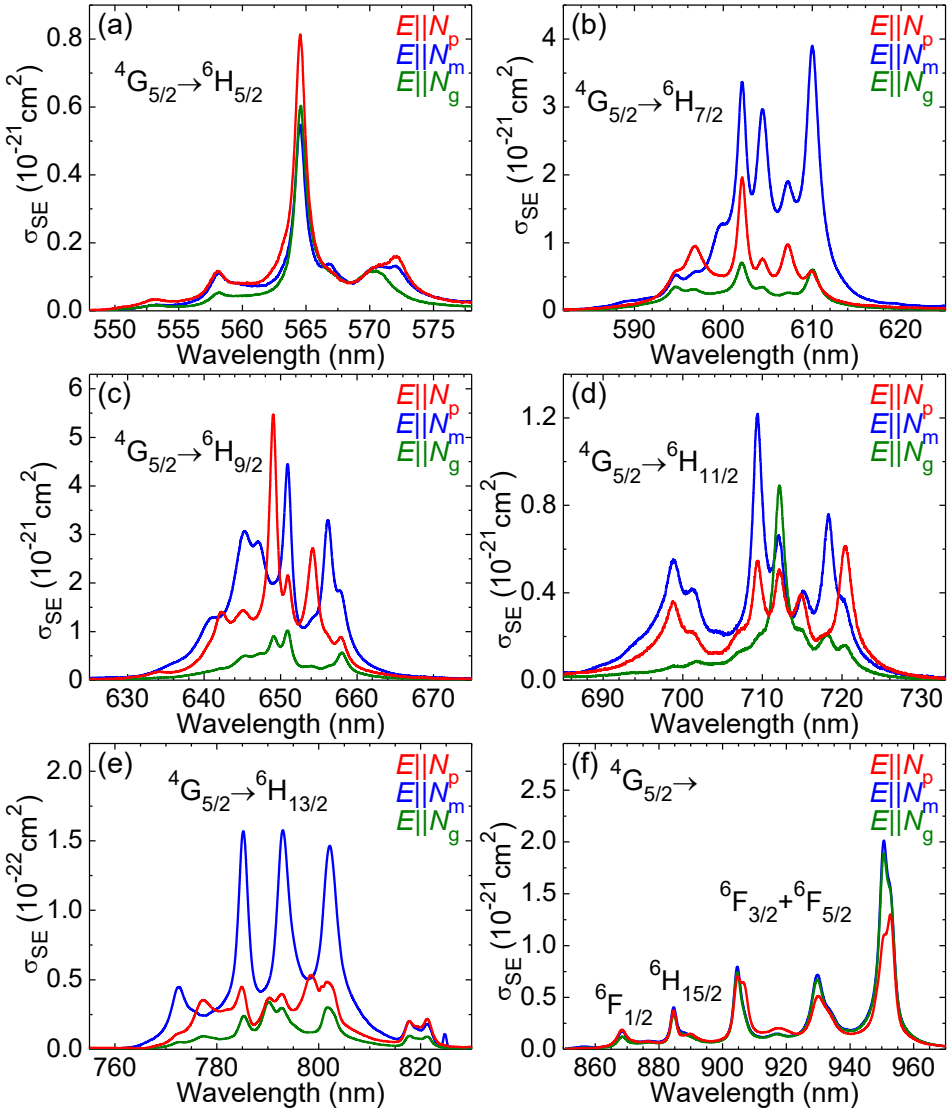

Figure 7. (a-f) Polarized stimulated-emission (SE) cross-section, σ_{SE}, spectra for transitions from the $^4G_{5/2}$ metastable state to the lower-lying ^6H_J and ^6F_J manifolds: (a) $^6H_{5/2}$, (b) $^6H_{7/2}$, (c) $^6H_{9/2}$, (d) $^6H_{11/2}$, (e) $^6H_{13/2}$, (f) $^6H_{15/2}$ and ^6F_J (J = 1/2, 3/2, 5/2), the light polarizations are $\boldsymbol{E} \parallel N_p$, N_m and N_g.

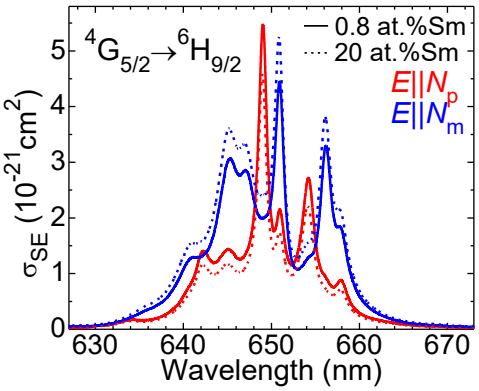

Figure 8. Comparison of stimulated-emission (SE) cross-sections, σ_{SE}, for the $^4G_{5/2} \rightarrow {}^6H_{7/2}$ transition for 0.8 at.% Sm^{3+}-doped (*solid lines*) and 20 at.% Sm^{3+}-doped (*dashed lines*) $KGd(WO_4)_2$ crystals. The light polarizations are $\boldsymbol{E} \parallel N_p$ and $\boldsymbol{E} \parallel N_m$.

Table 6. The peak emission wavelengths, λ_{em}, and stimulated-emission cross-sections, σ_{SE}, for selected transitions originating from the $^4G_{5/2}$ Sm^{3+} metastable state in the 0.8 at.% Sm:$KGd(WO_4)_2$ crystal. The corresponding light polarization is indicated in parentheses.

$^4G_{5/2}\rightarrow{}^{2S+1}L_J$	λ_{em}, nm	σ_{SE}, 10^{-21} cm²	Color
$^6H_{5/2}$	564.6	0.81 (*p*)	Yellow
$^6H_{7/2}$	610.0	3.91 (*m*)	Orange
$^6H_{9/2}$	649.0	5.47 (*p*)	Red
$^6H_{11/2}$	709.4	1.22 (*m*)	Deep-red
$^6H_{13/2}$	792.9	0.16 (*m*)	Deep-red
$^6F_{1/2}$	868.4	0.19 (*p*)	IR
$^6H_{15/2}$	884.6	0.41 (*m*)	IR
$^6F_{3/2}$+$^6F_{5/2}$	950.7	2.02 (*m*)	IR

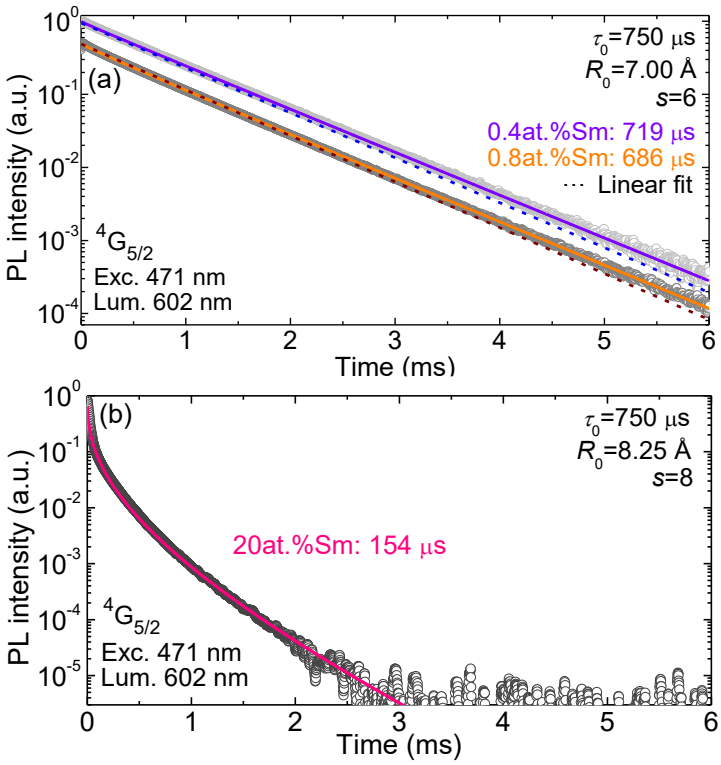

Figure 9. (a,b) Luminescence decay curves from the $^4G_{5/2}$ state of Sm^{3+} ions in $KGd(WO_4)_2$ crystals: (a) 0.4 at.% Sm^{3+} and 0.8 at.% Sm^{3+}; (b) 20 at.% Sm^{3+}. *Grey circles* – experimental data, *solid curves* – their fits using the I-H model. λ_{exc} = 471 nm, λ_{lum} = 602 nm.

Table 7. Einstein coefficients, B_{calc}, representing the probabilities of transitions in stimulated-emission (SE) and absorption (ESA) from the metastable $^4G_{5/2}$ Sm^{3+} state in the $KGd(WO_4)_2$ crystal. The calculations were performed using the modified Judd-Ofelt formalism. $\Delta E_{JJ'}$ corresponds to the energy difference between the two levels involved in the transition.

SE $^4G_{5/2}\rightarrow{}^{2S+1}L_J$	ESA $^4G_{5/2}\rightarrow{}^{2S+1}L_J$	Manifold energy $E_{J'}$, cm^{-1}	Transition energy $\Delta E_{JJ'}$, cm^{-1}	B_{calc}, 10^{-17} $m^3s^{-2}J^{-1}$	Color
$^4G_{5/2}\rightarrow{}^6H_{7/2}$		1260	16530	0.386	Orange
	$^4G_{5/2}\rightarrow{}^4F_{9/2}$	34240	16450	0.859	
	$^4G_{5/2}\rightarrow{}^2L_{17/2}$	34410	16620	0.010	
	$^4G_{5/2}\rightarrow{}^4I_{9/2}$	34430	16650	0.520	
$^4G_{5/2}\rightarrow{}^6H_{9/2}$		2460	15330	0.579	Red
	$^4G_{5/2}\rightarrow{}^4P_{5/2}$	32620	14830	0.395	
	$^4G_{5/2}\rightarrow{}^2F_{5/2}$	33510	15720	0.475	
$^4G_{5/2}\rightarrow{}^6H_{11/2}$		3770	14020	0.158	Deep-red
	$^4G_{5/2}\rightarrow{}^4G_{11/2}$	31640	13860	0.906	
	$^4G_{5/2}\rightarrow{}^2K_{15/2}$	31420	13630	2.037	
	$^4G_{5/2}\rightarrow{}^4P_{3/2}$	31520	13730	0.363	

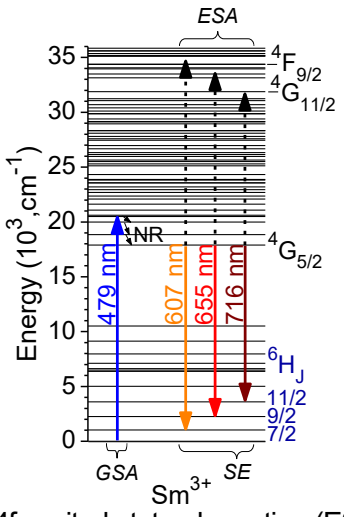

Figure 10. Possible 4f-4f excited-state absorption (ESA) transitions from the $^4G_{5/2}$ Sm^{3+} metastable state to higher-lying excited-states (*dashed arrows*), according to calculations within the modified Judd-Ofelt theory. *Solid arrows* – pump (GSA) and laser (SE) transitions.

Table 8. Fractional thermal populations of Stark sub-levels of the $^4G_{5/2}$ manifold of Sm^{3+} ions in the $KGd(WO_4)_2$ crystal.

Sub-level energy E, cm^{-1}	Fractional thermal population	
	T = 300 K	T = 400 K
17601	0.656	0.577
17876	0.176	0.215
17885	0.168	0.207

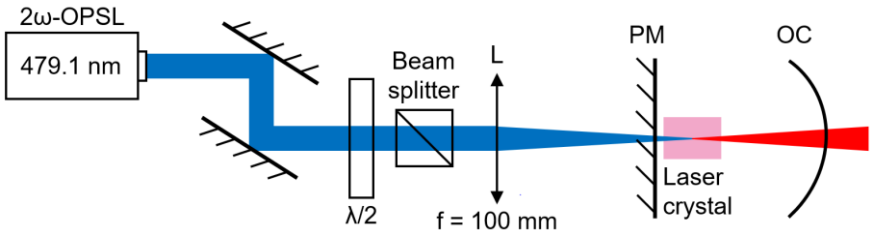

Figure 11. Scheme of the laser setup: L, AR-coated achromatic focusing lens; PM, pump mirror; OC, output coupler.

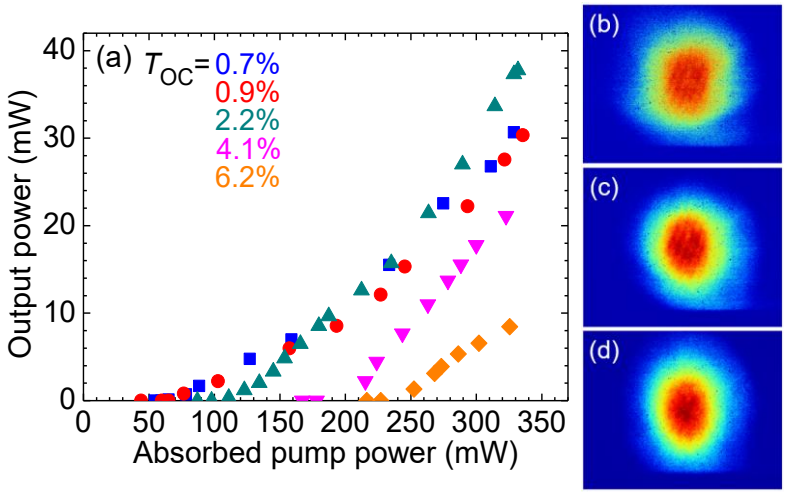

Figure 12. Output performance of the red 0.8 at.% Sm:KGd$(WO_4)_2$ laser emitting at 649 nm: (a) Input-output dependences; (b-d) far-field laser mode profiles captured at different output powers of the laser for T_{OC} = 4.1%: (b) near the laser threshold; (c) at ~10 mW; (d) at ~21 mW.

Table 9. Output characteristics of the red 0.8 at.% Sm:KGd$(WO_4)_2$ laser: T_{OC} – output coupling, P_{th} – laser threshold, η – slope efficiency, P_{out} – maximum output power.

T_{OC}, %	P_{th}, mW	η, %	P_{out}, mW
0.7	55	13.8	30.7
0.9	44	12.4	30.3
2.2	87	17.6	37.8
4.1	167	17.5	21.1
6.2	216	9.7	8.5